Optoperforation of Intact Plant Cells, Spectral Characterization of Alloy Disorder in InAsP Alloys, and Bimetallic Concentric Surfaces for Metal-Enhanced Fluorescence in Upconverting Nanocrystals

Travis R. Merritt

Dissertation submitted to the Faculty of the
Virginia Polytechnic Institute and State University
in partial fulfillment of the requirements for the degree of

Doctor of Philosophy
in
Physics

Giti A. Khodaparast, Chair
Mark L. Pitt
Hans D. Robinson
James H. Westwood

December 9, 2013
Blacksburg, Virginia

Keywords: optoperforation; laser-mediated plant cell disruption; alloy disorder; photoluminescence of III-V alloys; plasmonically enhanced emission; metal-enhanced absorption; upconversion; nanocolloid; interdisciplinary

Copyright 2013, Travis R. Merritt

Optoperforation of Intact Plant Cells, Spectral Characterization of Alloy Disorder in InAsP Alloys, and Bimetallic Concentric Surfaces for Metal-Enhanced Fluorescence in Upconverting Nanocrystals.

Travis R. Merritt

(ABSTRACT)

The techniques of optoperforation, spectral characterization of alloy disorder, and metal-enhanced fluorescence were applied to previously unconsidered or disregarded systems in order to demonstrate that such applications are both feasible and consequential. These applications were the subject of three disparate works and, as such, are independently discussed.

Despite being ostensibly restricted to mammalian cells, optoperforation was demonstrated in intact plant cells by means of successful femtosecond-laser-mediated infiltration of a membrane impermeable dextran-conjugated dye into cells of vital *Arabidopsis* seedling stems. By monitoring the rate of dye uptake, and the reaction of both CFP-expressing vacuoles and nanocellulose substrates, the intensity and exposure time of the perforating laser were adjusted to values that both preserved cell vitality and permitted the laser-assisted uptake of the fluorophore. By using these calibrated laser parameters, dye was injected and later observed in targeted cells after 72 hours, all without deleteriously affecting the vital functions of those cells.

In the context of alloy disorder, photoluminescence of excitonic transitions in two $InAs_xP_{1-x}$ alloys were studied through temperature and magnetic field strength dependencies, as well

as compositionally-dependent time-resolved behavior. The spectral shape, behavior of the linewidths at high magnetic fields, and the divergence of the peak positions from band gap behavior at low temperatures indicated that alloy disorder exists in the x=0.40 composition while showing no considerable presence in the x=0.13 composition. The time-resolved photoluminescence spectrum for both compositions feature a fast and slow decay, with the slow decay lifetime in x=0.40 being longer than that of x=0.13, which may be due to carrier migration between localized exciton states in x=0.40.

In order to achieve broadband metal-enhanced fluorescence in upconverting $NaYF_4$:Yb,Er nanocrystals, two nanocomposite architectures were proposed that retrofit metallic nanoshells to these lanthanide-doped nanocrystals. The typical monometallic construction was rejected in favor of architectures featuring Au-Ag bimetallic concentric surfaces, a decision supported by the considerable overlap of the calculated plasmon modes of the metallic structures with the emission and absorption spectrum of the nanocrystals. Furthermore, precursors of these nanocomposites were synthesized and photoluminescence measurements were carried out, ultimately verifying that these precursors produce the requisite upconversion emissions.

Acknowledgments

This work has been made possible by the support of a whole range of individuals and they deserve special recognition for that support.

Prof. Giti Khodaparast, my adviser, for her encouragement over the years, for allowing me to pursue a swathe of experimental endeavors, and for providing me with numerous opportunities to collaborate with a diverse group of individuals.

Prof. Jim Westwood and Prof. Tim Long; for their willingness to collaborate on interdisciplinary projects, and for their advice and contributions to those projects.

Prof. Hans Robinson, Prof. Mark Pitt, and Prof. Jim Westwood; for agreeing to be on my committee and for providing much needed advice and consent with regard to my doctoral work.

Dr. Steve McGill, you are the patron saint of patience and your guidance during our visits to the Magnet Lab led to the success of many experimental undertakings.

Megan LeBlanc and David Inglefield; you guys are brilliant individuals and working with you over the past couple of years has been an absolute pleasure. In fact, you have made the grueling slog of graduate work seem more like play than work.

Diane Walker-Green and Chris Thomas; for their advice and guidance, and for the great conversations that weve had over my long stay at Virginia Tech.

Jameel McMillan, Mike Meeker, Dr. Brenden Magill, and Alex Winemiller; for their assistance on a variety of projects.

My family: Mom, Dad, Kenlyn, Chelsea, Andy, Ginny, Parker, Grandma; for their love and support, and for instilling in me values that I cherish, such as curiosity, humor and empathy.

My adopted family: Adam, Jon, George, Amanda, Jenn, Addison, MJ, Heather, Sara, Rob, Carolyn, Josh, Adnama, Matt, David, Alma, Monica, Meredith; your friendship has been invaluable over the years and the bonds that we have forged will long and lasting. Each and everyone one of you have been role models for me and I aspire to be more like you all every day.

Attributions

Chapter 1: Authorship is equally shared with Megan LeBlanc. Jameel McMillan worked to design wash protocols and the project was overseen by both Dr. Giti Khodparast (Physics) and Dr. James Westwood (Plant Pathology, Physiology, and Weed Science). Manuscript was accepted by Optics Express on May 31, 2013 and editorially selected for the Virtual Journal for Biomedical Optics on August 1, 2013, in the form reproduced here.

Contents

List of Figures

List of Tables

Chapter 1

Introduction

1.1 Summary

The works presented here focus on using experimental techniques that have been well established and applying them to systems that have, thus far, been underrepresented or unconsidered in studies featuring those techniques. Hence, the common thread that binds these works is not the development of some neoteric procedure. Instead, it is the desire to seek out systems that have largely been overlooked and demonstrate that these established techniques are both feasible for and relevant to those systems. For two studies presented here, this task required dialogue between dissimilar disciplines and thus necessitated interdisciplinary participation. In contrast, the remaining study features a characterization of a system that has been, to a great extent, precluded from scientific inquiry.

The established methods featured in this work are optoperforation, spectral characterization of alloy disorder, and metal-enhanced fluorescence. Briefly, optoperforation is the laser-mediated modification of membrane permeability in a given cell used, generally, to encourage

the uptake of exogeneous molecules. While this technique has largely been demonstrated in mammalian cells, plant cells have rarely been considered, especially those of an intact organism. Regarding the second technique, spectral analysis of the excitonic emission in II-IV and III-V alloys can indicate the distribution of alloy components and, by extension, reveal the extent of exciton localization. Although many alloys have been subjected to such an analysis, studies that optically characterize InAsP alloys in the context of alloy disorder are lacking. Finally, metal-enhanced fluorescence is the metal-induced increase in the luminescence quantum yields of a fluorophore by resonant surface plasmon modes of nearby metallic structures. This method has been used to enhance the emission efficiency of lanthanide-doped upconverting nanocrystals by incorporating those nanocrystals into a nanocomposite containing a unitary metallic shell; however, bimetallic concentric nanosurfaces, which have the capacity to broadly enhance the upconversion process, have not been employed for such composites.

As the relevance of this thesis spans three disparate research topics, each chapter stands as a self-contained treatment of each topic. These chapters briefly introduce the primary technique, justify their application to a previously overlooked system, examine the results of this application, and, finally, discuss the challenges that remain.

In Chapter 2, optoperforation was used to inject a dye conjugate into a single cell of *Arabidopsis* seedling stems while maintaining cell vitality. The effects of focused femtosecond pulse trains on the physiological and morphological of the cells were monitored and laser parameters were adjusted to achieve benign laser-mediated infiltration of the fluorophore into a targeted cell. Long term dye retention was accessed as well as dye-uptake dynamics.

In Chapter 3, spectral- and time-resolved photoluminescence of InAsP ternary alloys were used to determine the extent of alloy disorder in two compositions. This was achieved, primarily, by examining the magnetic field and lattice temperature dependencies of the peak

positions and linewidths of excitonic radiative recombinations. Furthermore, the temporal behavior of these recombinations was measured and discussed in the context of exciton localization.

In Chapter 4, nanocomposites containing both lanthanide-doped upconverting nanocrystals and concentric bimetallic structures were proposed for the metal-induced enhancement of the upconversion emissions. Precursors for these composites were fabricated and their photoluminescence spectra were measured. In addition, the resonant plamon modes of the bimetallic nanocomposites were calculated and their enhancement potential on the upconversion emissions was examined.

In Chapter 5, these works were reviewed and their outcomes were discussed. In addition, future undertakings were proposed for each work that would either address unfinished research or provide motivation for future investigations.

1.2 Contributions to other published works

While the studies presented in the following chapters constitute the majority of my graduate work, I was involved in a number of other experimental efforts. However, my participation in those endeavors was minimal and, as a result, did not warrant a thorough treatment in this thesis. However, I include a brief summary below detailing my role in those experiments to serve as a simple chronicle of my other research experiences.

1.2.1 Pump-Probe Spectroscopy

In the following works, pump-probe methods were used to characterize the dynamical behavior of nonequilibrium carriers in a variety of ferromagnetic and nonferromagnetic InAs- or

InSb-based epitaxial films and quantum wells [1, 2, 3, 4, 5, 39]. To this end, the photoexcited spin and carrier lifetimes of these systems were determined by time- and spin-resolved differential transmission measurements. In addition, these lifetimes were measured as a function of a variety of experimental factors: growth parameters, lattice temperature, pump fluence and external magnetic field strength. This latter dependency was relevant for the ferromagnetic films and typically required high magnetic fields, which prompted many visits to National High Magnetic Field Lab in Tallahasee, Florida [3, 5, 39].

For these studies, my role was predominately one of technical support for the optical aspects of the various pump-probe schemes, which typically involved constructing portions of the optical setups and aligning the pump and probe beams. However, this role slightly differed in the 2009 study [2], where we attempted to perform cyclotron resonance (CR) measurements on InMnAs films to determine effective mass and, by extension, energy dispersion of the carriers. However, due to the low mobility of the carriers, these measurements required high magnetic fields and, by extension, the use of the pulsed magnetic facilities at the High Magnetic Field Laboratories in Dresden, Germany. There, I was tasked with preparing the samples for the pulsed magnet sample chamber. Unfortunately, CR was not observed in these films for magnetic fields produced by this pulse system (<50 T) [2].

Published works

K. Nontapot, R.N. Kini, A. Gifford, T.R. Merritt, G.A. Khodaparast, T. Wojtowicz, X. Liu, and J.K.Furdyn, *Relaxation of Photoinduced Spins and Carriers in Ferromagnetic InMnSb Films,* App. Phys. Lett. **90**, 143109 (2007).

M. Bhowmick, T. R. Merritt, K. Nontapot, B. W. Wessels, O. Drachenko, and G. A. Khoda-

parast, *Time Resolved Spectroscopy of InMnAs Using Differential Transmission Technique in Mid-Infrared,* Phys. Procedia **3**, 1167 (2009).

M. Bhowmick, T.R. Merritt, G.A. Khodaparast, C. Feeser, B.W. Wessels, S.A. McGill, D. Saha, X. Pan, G. D. Sanders, and C. J. Stanton, *Time Resolved Spectroscopy of MOVPE Grown Narrow Gap Ferromagnetic Semiconductors,* AIP Conf. Proc. **1416**, 188 (2011).

M. Bhowmick, T.R. Merritt, K. Nontapot, G.A. Khodaparast, T. D. Mishima, and M.B. Santos, *Carrier Dynamics in Parabolic InSb Based Multi Quantum Wells*, AIP Conf. Proc. **1416**, 192 (2011).

M. Bhowmick, T. R. Merritt, G. A. Khodaparast, B.W. Wessels, S.A. McGill, D. Saha, G.D. Sanders, and C.J. Stanton, *Time-resolved differential transmission in MOVPE-grown ferromagnetic InMnAs,"* Phys. Rev. B **85**, 125313 (2012).

M.A. Meeker, B.A. Magill, T.R. Merritt, M. Bhowmick, K. McCutcheon, G.A. Khodaparast, J.G. Tischler, S. McGill, S.G. Choi, C.J. Palmstrm, *Dynamics of photoexcited carriers and spins in InAsP ternary alloys,* App. Phys. Lett. **102**, 222102 (2013).

1.2.2 Cyclotron Resonance in Ferromagnetic InMnAs and InMnSb Films

In order to obtain any observable CR in the previously discussed InMnAs films, as well as in InMnSb films, a higher peak magnetic field strength was required. As such, we performed

CR measurements at the International MegaGauss Science Laboratory at the University of Tokyo, with facilities capable of generating the requisite fields (>100T) [6]. In order to produce these fields, we relied on a destructive single-turn coil method, whereby a megaampere current is injected into a single-folded coil which achieves high fields at the cost of destructive Maxwell stresses. Using these high fields in conjunction with CO_2, CO, and H_2O lasers as infrared excitation sources, CR measurements were performed and later combined with effective mass theory calculations to determine the complex band structure and exchange parameters of the ferromagnetic systems.

My participation in this work consisted of preparing and inspecting the single-turn coils and expendable cyrostats, and, after each CR measurement, cleaning the explosion chamber of debris and replacing the ravaged components.

Published work

G. A. Khodaparast, Y. H. Matsuda, D. Saha, G. D. Sanders, C. J. Stanton, H. Saito, S. Takeyama, T. R. Merritt, C. Feeser, B. W. Wessels, X. Liu, and J. Furdyna, *Cyclotron resonance in ferromagnetic InMnAs and InMnSb*, Phys. Rev. B (*under review*).

1.2.3 Spectral Characterization of Ge Epitaxial Layers

The work below represents a collaboration between our research group and Mantu Hudait's group in the Electrical Computer Engineering Department of Virginia Tech [7]. While this study is largely concerned with the interfaces in MBE-grown GaAs/Ge/GaAs heterostructures and their effect on the morphological and electrical properties of these structures, the study also considers the optical properties of these heterostructures in order to ascertain the quality of the Ge epitaxial layer. The reason for this inclusion is that the proportional

representation of the direct and indirect band gap transitions in the emission spectrum is dependent on both the n-type doping and interfacial biaxial tensile strain. The weak direct band gap transition observed at room temperature is indicative of the low unintentional doping in the Ge layer and thereby attests to its high quality.

I contributed to this work in a supplementary capacity by performing cryogenic and room temperature photoluminescence measurements on these heterostructures.

Published work

M.K. Hudait, Y. Zhu,N. Jain, S. Vijayaraghavan, A. Saha, T.R. Merritt ,G.A. Khodaparast, *In situ grown Ge in an arsenic-free environment for GaAs/Ge/GaAs heterostructures on off-oriented (100) GaAs substrates using molecular beam epitaxy.* J. Vac. Sci. Technol. B **30**, 051205 (2012).

This paper is published in *Optics Express* and *Virtual Journal for Biomedical Optics*, and
is under copyright of OCIS. Systematic or multiple reproduction or distribution to multiple locations via electronic or other means is prohibited and is subject to penalties under law.

Chapter 2

Optoperforation of single, intact *Arabidopsis* cells for uptake of extracellular dye-conjugated dextran.

T. R. Merritt[1], J. McMillan, G. A. Khodaparast*
Department of Physics, Virginia Tech, Blacksburg, VA 24061, USA

M.L. LeBlanc[1], J.H. Westwood
Department of Plant Pathology, Physiology, and Weed Science, Virginia Tech, Blacksburg, VA 24061

[1]These authors contributed equally to this work.
(*,**)Authors to whom correspondence should be addressed; electronic addresses: *westwood@vt.edu and **khodapar@vt.edu.

Keywords: laser-mediated optoperforation; cascade blue; fluoroscein; dextran; *Arabidopsis*; multiphoton events; confocal microscopy.

Abstract

A plant science research goal is to manipulate single cells in an intact organism in order to study their interactions with neighboring cells. Based on a technique previously demonstrated in isolated plant cells, mammalian cells and cyanobacteria, *Arabidopsis* epidermal cells were optoperforated to allow for uptake of external cascade blue-labeled dextrans. Adverse organelle responses were determined to be minimal and dye retention was demonstrated for at least 72 hours. This technique overcomes the physical challenges presented by the plant cell wall and demonstrates the feasibility of *in situ* optoperforation.

2.1 Introduction

Optoperforation (OP) can be found in scientific literature under many names: nanoinjection, optical injection, phototransfection, photoporation, or micropuncture; all of which refer to the technique of using lasers to form a quasi-free electron plasma at a cellular boundary to increase its permeability, ultimately allowing uptake of materials from a solution surrounding the cell [8]. Optical cellular manipulation has been applied to mammalian cells for ophthalmic surgery as long ago as the 1960s [9]. Unfortunately, plant science has been unable to utilize this technique in intact plant systems due the unyielding nature of the plant cell wall and the difficulty in maintaining a living plant during and after the procedure in vitro. Instead, cultured and protoplast cells have been the subjects for a number of optoperforation studies, many of which used this optical approach as a replacement for the otherwise cumbersome techniques available for the introduction of transgenes, such as biolistics or *Agrobacterium*-mediated transformation.

A principle that many optoperforation experiments exploit is a difference in tonicity between

the intra- and extra-cellular domains that allows for a concentration gradient, which facilitates movement from one region to the other. For example, UV-laser irradiated *Brassica napus* cultures in hypertonic solution with a β-glucuronidase (gusA) expressing construct had a 50% survivability rate of perforated cells two days post laser exposure and gusA expression was detected in 71% of survivors after 4 days [10]. Cultured cells of *Brassica napus* have been shown to remain viable following UV (343 nm, 15 ns) laser irradiation followed by uptake of bizbenzimide-labelled pBR322 plasmid, with cytoplasmic streaming visible one hour post treatment and similar survival rates [10]. Cultured wheat cells were also transformed with a gusA expression vector by a UV laser (6 ns, 308 nm with pulse energies up to 13 mJ) with confirmation of transformation seen in 3 out of 600 samples [11].

In addition, pollen has been used for laser mediated transformation due to its ease of culture, but transfection efficiency was low [12]. Specifically, *Lilum hybrid* pollen walls were perforated with an energy density of 1.42 J/cm^2 at 0.6 ms from a near infrared (NIR) laser (Ti:Sapphire, 1kHz) and infiltrated with a mitochondrion-targeted red fluorescent protein construct [13]. Atomic force microscopy showed formation of a hole 1.1 μm wide and 0.9 μm deep, and overall transformation efficiency was only 4.4%, slightly higher than the 4.1% efficiency typical for biolistics methods [14].

Protoplasts of *Nicotiana tabacum*, Bright Yellow-2 (BY-2), were subjected to 1064 nm (Nd:YAG) picosecond pulses with energies <5 mJ and were found to take up peroxisome-localized Yellow Fluorescent Protein (YFP) [15]. Fluorescence was detected 22 to 48 hours post irradiation in five out of 200 cells (2.5% efficiency). A recent experiment using *Anabaena* cyanobacteria was the first to demonstrate bacterial cell wall penetration using femtosecond laser pulses in the presence of gold nanoparticles, which increase the localized electromagnetic field of the laser and allow perforations to occur at lower pulse energies and shorter pulse trains than previous attempts [16].

Laser mediated incorporation of a post transcriptional gene silencing signal, such as siRNA, is another technique with value to plant science. Callus cultures of three species, slash pine (*Pinus elliottii*), cotton (*Gossipyum hirsutum*) and rice (*Oryza sativa*), which had each been transformed to express Green Fluorescent Protein (GFP), were used to test uptake of a GFP siRNA construct [17]. The calli were subjected to a laser induced stress wave (LISW) originating from a rubber sheet adjacent to the tissue, which caused the affected calli to become permeable to the siRNA construct. This resulted in stable silencing of GFP expression starting as early as five days post LISW and lasting for greater than two months, with a total efficiency of 80-95% silencing [17].

Although optoperforation may substitute for other methods of single cell manipulation, the true value of the technique is in manipulating specific cells of intact plant organs instead of callus and protoplasts. We could find no reports of the manipulation of cells in living, intact plants using optoperforation, possibly because the cell wall is too difficult to breach or because whole-mounted plant samples are cumbersome to image and maintain over time. Successful incorporation of a known molecule into a single cell of a plant would be ideal for characterizing trafficking through plasmodesmata or for studying intracellular localizations. Here we show NIR femtosecond laser-mediated infiltration of a membrane impermeable dextran-conjugated fluorophore into cells of live *Arabidopsis thaliana* seedling stems, along with data on the laser effects to cellular structures. This method is ideal for studies of cell-to-cell interactions and potentially paves the way for introducing transgenes to specific cells within a plant.

2.2 Materials and methods

2.2.1 Plant preparation

Arabidopsis thaliana (cv. Colombia) seeds were plated on Murashige and Skoog (MS) + sucrose media [18] and grown in 12 hr light/dark cycles for 1 week. Seedlings were prepared for laser irradiation and dye uptake as described in Weber, *et al.* [19] by submersion in 1X phosphate buffered saline (PBS) with either a control solution containing 50% v/v 70 kDa dextran-fluorescein (Life Technologies Co.) or a treatment solution of 50% 10 kDa dextran-cascade blue (Life Technologies Co.) in a glass bottomed 35 mm dish (Mattek Co., P35G-1.5-20C) and covered with a plastic coverslip. Transgenic *Arabidopsis* plants expressing vacuole-targeted Cyan Fluorescent Protein (CFP) [20] were used for laser refractory tests. Following the optoperforation procedure, plants were rinsed with sterile distilled water with minimal movement of the overlying coverslip. Water supplemented with 50% $\frac{1}{4}$X Hoaglands Solution [21] was introduced under the coverslip, and the housing dish was capped with a lid and sealed with parafilm to prevent desiccation.

2.2.2 Optoperforation apparatus

The laser source used for both the fluorescence imaging and optoperforation portions of this work was a Kerr lens mode locked Ti:Sapphire laser (Chameleon, Coherent Inc. Santa Clara, CA) operating in a wavelength range of 690-1064 nm with a pulse duration of approximately 140 fs, a repetition rate of 80 MHz, and a TEM00 spatial mode. Before being coupled to the laser port of a confocal laser scanning microscope (Zeiss LSM 510, Carl Zeiss Inc., Thornwood, NY), the laser pulses pass through an acousto-optical modulator, providing both laser beam attenuation and beam-blanking. After arriving at the laser port, the pulses

continued onward to a galvano scanning mirror unit, then to a 660 nm edge short-pass dichroic beam splitter, and were finally focused on a sample by a telecentric water-immersed objective lens (NA 1.2 /40x, Carl Zeiss MicroImaging, Inc. Thornwood, NY). Laser power was measured at the sample plane.

2.2.3 Fluorescence microscopy and image processing

In order to measure the fluorescence of either nonreactive dye or fluorescent proteins, a multiphoton (MP) excitation configuration was used. To monitor cascade blue (CB) uptake, the sample was excited by 750 nm at 20 mW (2.6×10^{12} W/cm^2), the ensuing fluorescence was collected by the objective, and passed through the dichroic mirror and a 427/37 nm (CWL/BW) bandpass filter. Similarly, the fluorescence of CFP was observed by exciting the sample with 840 nm at 25 mW (2.6×10^{12} W/cm^2) and passing said fluorescence through the dichroic mirror and a 487/44 nm bandpass filter. Images were captured by a PMT and processed by the LSM software (©Carl Zeiss Microimaging, GmbH. 1997-2006) on a PC. Efficacy of dye retention was determined by measuring the differential fluorescent intensity between targeted and untargeted cells. For time-lapse analysis of CB uptake, the fluorescence intensity was integrated over a region enclosed by the monitored cell.

2.2.4 Optoperforation protocol

A glass bottom dish containing the *Arabidopsi*s seedling was mounted on the cross-slide stage of the microscope, and the horizontal movement of the stage was actuated manually by a coaxial drive. A built-in piezoelectric step motor in the microscope controlled the vertical position of the objective and, by extension, the focal point. Through this motion control, the positions of the dish and objective were adjusted until the cells closest to the glass interface

were visualized in bright field images. At this point, cells of the stem epidermal layer that were in contact with the surrounding medium and had a uniform structure that were amenable to visualization were targeted. The Z position of the objective was adjusted until a cell wall surface was in the focal plane (only cell walls salient to the surrounding solution were targeted in this work). Then the injection site was selected and its XY position was recorded using the spot scan feature of the Zeiss software, which directs the laser at a desired point in the focal plane during the scan process. This is in contrast to a planar scan, where the entire focal plane is scanned in a raster pattern. Once the injection site was acquired, the objective was moved 1.5 μm below the cell wall plane. The laser was then directed at the specified XY location, exposing that location to a given perforation power for a pulse train duration of 0.64 μs. Following laser exposure, a planar image was immediately taken. The objective was moved upwards in 0.5 μm increments, repeating the exposure-scan procedure for each increment until either a notable response from the cell to the perforating laser was observed or the objective moved a total distance of 3 μm. Approximately 10 seconds transpired between successive exposures, which comprised of the time needed to reposition the objective and to monitor for cellular responses to the perforating laser exposure in images taken immediately after exposure. This procedure was applied to additional cells of the same *Arabidopsis* stem such that the total number of cells targeted on the same plant ranged from 5 to 10. For time lapse analysis of the optoperforation process, the protocol was the same except instead of capturing a solitary planar image immediately after injection, planar images were taken continuously for five minutes. From these images, the temporal development of CB uptake was determined by measuring the average fluorescence intensity in a region of interest confined to the perforated cell.

2.2.5 Post-optoperforation measurements

For ascertaining cell viability and long term dye retention, cells were imaged from 24 to 72 hours following the optoperforation event. As there is damage to the external cell wall we must be sure that the structural integrity is not so weakened as to damage the internal plasma membrane or that a breach of the apoplastic space is so severe as to cause cell death. Planar image stacks in increments of 1 μm were taken of regions encompassing targeted cells. Cells were visually inspected for general vitality and morphological changes induced by the optoperforation process. In addition, for cells containing CB within the confines of their cell wall, the distribution of the fluorophore was quantified. In addition, Scanning Electron Microscopy (SEM) for determining cell wall structural changes due to optoperforation was carried out on a Quanta 600 FEG system (FEI, Hillsboro, OR, USA).

2.3 Results and Discussion

2.3.1 Optoperforation mechanisms for intact plant cells

To explain the mechanisms responsible for femtosecond laser optoperforation, we rely on the theoretical framework proposed by Vogel *et al.* [22]. In this framework, when femtosecond laser pulses are tightly focused on a cell in an aqueous environment, sufficiently high intensities can be produced in the focal volume, around 10^{12} W/cm^2 in the focal plane, such that quasi-free electrons are generated through multiphoton ionization and subsequent avalanche ionization as shown in Figs. 2.1(a)-2.1(b). Since such requisite intensities are only found within the focal volume, the generated quasi-free electron plasma is relegated within this volume. At optimum densities, this plasma reacts photochemically with the cell wall and plasma membrane, dissociating biomolecules (such as lignin, cellulose, or phospholipids) to

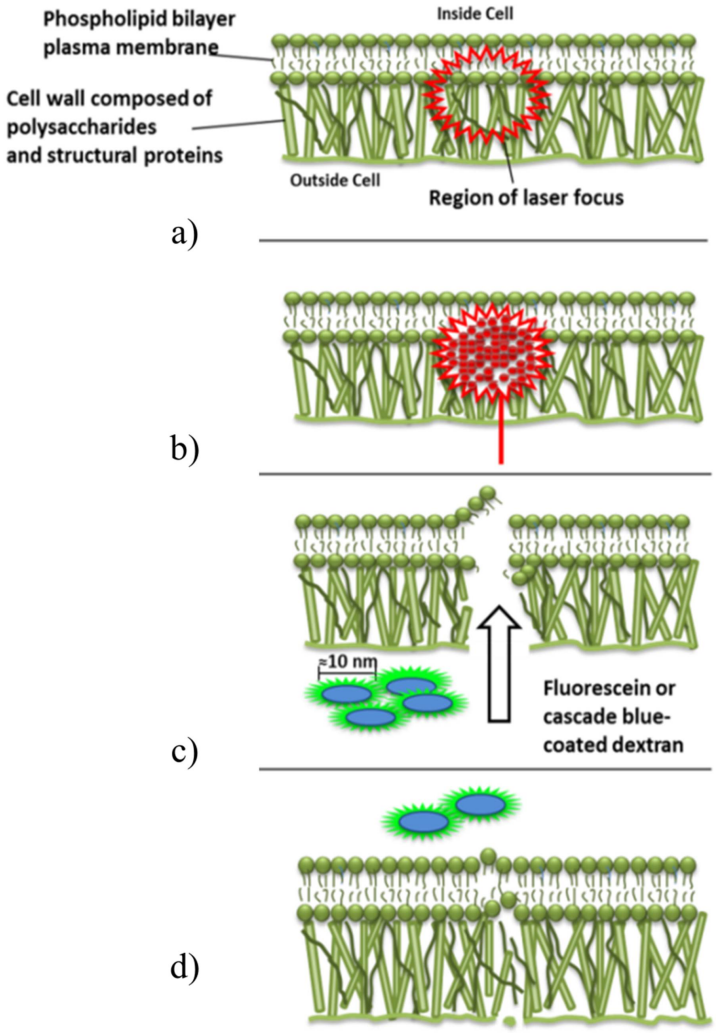

Figure 2.1: Diagram of the proposed mechanism by which laser-induced plasma formation could disrupt plant cell wall and plasma membrane, allowing for uptake of fluorophores through a transient pore. (a) Representation of cell structure within intact plant tissue at the site of laser focus. (b) Approximation of ideal laser ablation. (c) Broken cell wall and perforated plasma membrane allow external macromolecules to flow into the cellular space along a concentration gradient. (d) The transient nature of the plasma membrane pore allows it to re-seal, leaving slight damage to the cell wall but internalization of extracellular material.

create a pore, as demonstrated in Figs. 2.1(c)-2.1(d).

As the free electron density increases, cumulative heating and thermoelastic stress effects emerge, resulting in cavitation bubble formation and tensile shockwaves. As such, to achieve spatial accuracy of pore formation and avoid collateral cell damage, laser intensities must operate below the point in which cavitation bubbles emerge, referred to as the optical breakdown threshold, while still achieving sufficient plasma formation for pore creation described in the following sections.

In order to compare this work to the aforementioned theoretical findings and prior femtosecond OP works, our optoperforation results should be described in the context of laser irradiance at the focal plane. We approximate the spatial irradiance distribution in this plane as Gaussian, as presented in Eq. 2.1.

$$I(r,z) = I(0,0)\exp[-2(\frac{r^2}{\alpha^2} + \frac{z^2}{\beta^2})] \tag{2.1}$$

where r and z are the coordinates in the radial and axial directions, respectively, $I(0,0)$ is the on-axis, in-plane irradiance, and α and β are the lateral and axial radii at the $1/e^2$ irradiance level, respectively. For very large solid angles [23], the ratio between α and β is given by Eq. 2.2 as follows:

$$\frac{\beta}{\alpha} = \frac{(3 - 2\cos\theta - \cos 2\theta)^{\frac{1}{2}}}{1 - \cos\theta} \tag{2.2}$$

where θ is the focusing angle of the objective. For a water-immersed objective with NA=1.2, θ=64.5°, resulting in β/α=2.92. The measured average power, P_{avg}, can be related to the peak on-axis irradiance at z=0, I_{peak}=(0, 0), by Eq. 2.3:

$$I_{peak}(0,0) = \frac{2P_{peak}}{\pi\alpha^2} = \frac{2P_{avg}}{\nu\tau\pi\alpha^2} \tag{2.3}$$

where ν is the repetition rate of the laser, τ is the laser pulse duration, and α is the $1/e^2$ lateral radius.

Due to temporal broadening of the confocal system, the pulse duration will be larger than the 140 fs initially produced. According to the manufacturers specifications, the confocal system incurs a group-delay dispersion at 750 nm of approximately 7500 fs^2, providing a broadened pulse duration of $\tau\approx$200 fs [24].

The $1/e^2$ lateral diameter of the image spot from a truncated Gaussian input beam passing through a diffraction-limited lens is given by [25],

$$d = K_{1/e^2} \cdot \lambda \cdot f/\# \tag{2.4}$$

where K_{1/e^2} in Eq. 2.4 is a constant that depends on the truncation ratio, λ is the wavelength of light, and $f/\#$ is the f-number of the objective. The truncation ratio is defined as $T{=}D_B/D_L$, where D_B is the $1/e^2$ diameter of the input beam and D_L is the diameter of the limiting aperture of the objective. In our system, the truncation ratio was measured to be 0.77 (which corroborates our assumption regarding the Gaussian focal-plane irradiance distribution), ultimately giving a K_{1/e^2} of 1.64 [25]. For NA=1.2, the corresponding f-number is 0.24. Since $\alpha{=}d/2$, α=180 nm. Since β/α=2.92, β=520 nm. Hence, the average powers used in this study, ranging between 5-100 mW, correspond to on-axis peak intensities in the range of 6.4×10^{11} to 1.3×10^{13} W/cm^2

From the irradiance distribution, the plasma density distribution can be approximated. Treating the water as an amorphous semiconductor with a band gap of 6.5 eV and noting

that the photon energy of the 750 nm perforation source is 1.65 eV, multiphoton ionization of water occurs in this case by the simultaneous absorption of 4 photons. Suggested by Vogel *et a*l. [22] the plasma density is proportional to I^k, where k is the number of photons required for multiphoton ionization; therefore, the $1/e^2$ radius for the plasma distribution should be smaller than that of the irradiance distribution by a factor of 2. Hence, the $1/e^2$ lateral and axial radii of the plasma distribution are 90 nm and 260 nm, respectively.

Due to the fact that the OP mechanics are confined within the focal volume, precisely co-aligning the focal plane with the cell wall is paramount. In fact, a misfocus of a Gaussian beam by as little as 3 μm was shown to reduce the efficacy of OP-mediated transfection by more than 50% [26]. To address such concerns, we adopted an OP protocol that relied on stepwise focal adjustments whereby a 3 μm long axial section centered on the cell-wall plane was exposed to a given perforation intensity at discrete 0.5 μm steps, as described above. While this approach exposes targeted cells to more optical doses, we did not observe a reduction in cell viability as a result of using this method. This is possibly due to the small volume in which the free-electron plasma is formed. Since the $1/e^2$ axial radius of the plasma distribution is 260 nm, the 0.5 μm separation between the exposure points of the perforating laser is approximately twice the plasma $1/e^2$ axial radius. Hence, the separation ensures that a given volume is not subjected to the effects of low-density plasma multiple times.

In addition to this stepwise approach, the imaging scheme also had a role to play in both the efficacy and evaluation of the OP process. Our approach requires an imaging scheme that both properly visualizes the interface between the cell wall and exogenous fluorescence medium during the initial targeting of a cell, and is capable of visualizing a cell embedded in a relatively thick tissue post-OP to determine fluorescent dye retention. These tasks can be confounded by out-of-focus fluorescence obscuring in-plane emissions, which is a particular

shortcoming of single-photon excitation imaging. To address this issue, an imaging scheme based on two-photon excitation (TPE) was used, whereby two NIR photons are simultaneously absorbed in a non-resonant fashion. Since this process can occur only within the focal volume where the photon density is sufficiently high, TPE does not suffer out-of-focus fluorescence scattering. In addition, TPE possesses a large Stokes shift to allow proper optical filtering of the excitation source from the ensuing emissions, suffers less attenuation due to a reduced scattering cross section, and enjoys improved depth discrimination compared to its single photon counterpart [27]. In contrast to previous reports where OP success was determined by monitoring endogenous fluorescence in isolated cells, depth discrimination is particularly important for our thick specimens.

While the infrared tunability of the Ti:Sapphire laser offers the ability to use a swathe of visible-emitting fluorophores, CB in particular was included in the hypertonic solution to monitor the diffusion of exogenous material into the cell upon the optical creation of a pore. Since the two-photon absorption cross section of CB indicates that this dye is readily excitable by 750 nm [28], the same wavelength was useful for both optoperforation and imaging of fluorescent dye infiltration. Hence, the laser cavity required no adjustment when these two functions were performed in succession, allowing immediate imaging of the cell after exposure to a perforating laser pulse train. In addition, the high energy emission of CB avoids the issue of emission cross-talk with autofluorescence sources such as lignin, cellulose and plastids. In summary, both the OP effect and the imaging scheme rely on mulitphoton effects and are differentiated as such: The OP effect relies on the simultaneous absorption of 4 photons by the aqueous media surrounding and residing within the targeted cell, while the imaging scheme relies on the simultaneous absorption of 2 photons by the dextran-conjugated cascade blue fluorophore.

To ensure that the infiltration of this nonreactive dye into a targeted cell was solely due to the

OP process, the dye was linked to membrane-impermeable dextrans and a series of control experiments were performed. Unbound fluorescent dyes, such as CB and fluorescein, are small enough to be taken up through the root vasculature and spread throughout the plant. Conjugation to a dextran of sufficient size prevents this passive diffusion. For instance, intact stem and root cells take up fluorescein-tagged dextran molecules up to 10 kDa (not shown); in contrast, 10- and 70 kDa dextrans proved to be non-diffusible and, as such, were used for these studies. Due to dextran conjugation, dye uptake was not observed in the absence of a perforating laser. Only cells exposed to the OP protocol showed measurable CB fluorescence within the confines of the cell wall. Furthermore, this intracellular CB fluorescence was due to the presence of dye, as no CB fluorescence was observed from cells subjected to the OP protocol that were in a medium devoid of CB.

In order to measure destructive laser ablation effects on the cell wall, we applied the OP technique to a TEMPO-oxidized nanocellulose material with properties similar to the natural cell wall [29]. Treated material was imaged by SEM to determine the size of the hole generated, indicating that an incident irradiance of 4.6×10^{13} W/cm^2 lasting 5.1 ms produced an ablation area 37.8 μm in diameter with a clearance hole of 6.3 μm, as shown in Fig. 2.2. Following this laser exposure, long-lived vapor bubbles with diameters >10 μm were observed and lingered for several seconds before their dissipation. The presence of these bubbles indicates that thermal accumulation effects are largely responsible for the scope of the observed damage, particularly when considering the 180 nm spot size of the laser. Regarding OP use on mammalian cells [22], the OP laser parameters used here correspond to the onset of immediate cell death in those studies. However, since the typical dimensions of a plant cell can be as little as 10 μm wide and up to 100 μm long, we would expect this cell death onset for *Arabidopsis* cells at much lower irradiances and reduced exposure times. The latter parameter is more important in this regard due to its integral role in accumulated

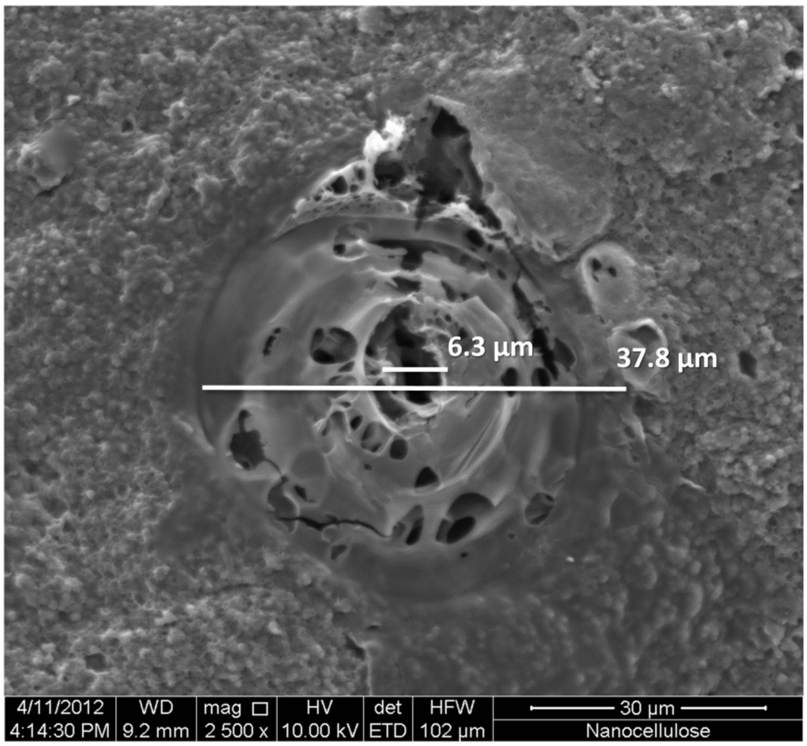

Figure 2.2: Scanning electron microscope image of the hole and peripheral effects generated at 4.6×10^{13} W/cm^2 irradiance for 5.1 ms exposure time in PCA-TEMPO nanocellulose (2500X magnification).

thermal effects. Hence, these findings warranted reducing the exposure time by more than three orders of magnitude to 0.64 μs.

Considering an OP procedure that preserves cell vitality, we must determine the laser irradiance threshold that demarcates destructive and non-destructive perforations. Indicators of the former kind are the byproducts of localized high plasma densities, such as transient cavitation bubbles and observable damage beyond the focal volume due to thermoelastic tensile stress waves. However, as the perforation laser irradiance is reduced toward the threshold level, the presence of these indicators is diminished to the point where the vitality of the cell is compromised without the aforementioned visual cues in brightfield images. As shown in

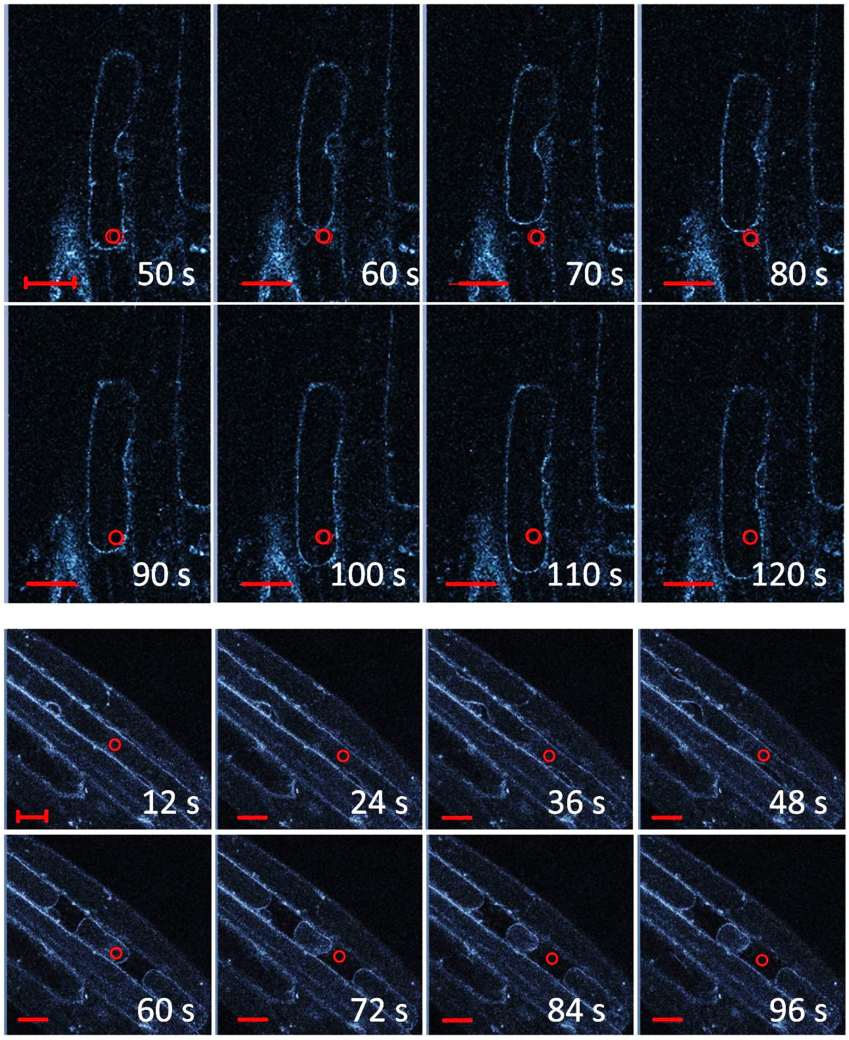

Figure 2.3: Timecourse images of *Arabidopsis* expressing CFP targeted to the vacuole membrane (indicated here by blue false-coloring). (a) Over a two minute time period following a 1.2×10^{13} W/cm^2 laser exposure, the vacuole shrinks and then rebounds (Media 1), possibly due to a rapid incursion of exogenous material. (b) Exposure to the same laser irradiance causes the vacuole to contract and break into three discrete units (Media 2), indicating that cell viability has been compromised. Red circle = site of laser scan. Bar = 20 μm.

Fig. 2.3, in order to avoid these surreptitious effects and ascertain the threshold in which they occur, we observed in real time the impact of laser irradiances on the integrity of the cell vacuole by monitoring the fluorescence from *Arabidopsis* plants expressing CFP on the vacuole surface, indicated by blue false-coloring in Fig. 2.3, the vacuole either shifted and

retracted away from the perforation site, indicating a rapid incursion of exogenous material, in case of Fig. 2.3(a) and Media 1, or split and reformed into discrete compartments as shown in Fig. 2.3(b) and Media 2. The observed damage to the vacuole corresponded to leakage of the infiltrated dye and cell death, indicating that the long-term integrity of the plasma membrane was compromised. For irradiances at or above 1.0×10^{13} W/cm^2, the vacuoles in 12 out of 13 cells displayed adverse reactions to the perforating laser similar to those shown in Fig 2.3. For irradiances at or below 9.0×10^{12} W/cm^2, no response by the vacuole was observed in all 11 cells that were targeted.

Exchange of contents between the cytoplasm and the surrounding solution was observed for irradiances above 5.3×10^{12} W/cm^2 (data not shown), implying that pores of sufficient size are produced above this lower bound. Hence, we conclude that optimum perforation irradiances lie in the range of 5.3×10^{12} - 9.0×10^{12} W/cm^2. An optoperforation was deemed successful if 72 hours after an OP event, a targeted cell displayed both CB retention within its cellular boundary and vital morphological criteria, such as cytoplasmic streaming and other normal cellular functions. For instance, eight cells, denoted by asterisks in Fig. 2.4(a), were targeted in a plantlet, and after 72 h fluorescence emissions were detected in six of those cells, as shown in Figs. 2.4(b)-2.4(c). Hence, for this set of cells, OP efficacy is approximately 85%. Overall OP efficacies were determined from the total number of cells exposed to a given perforating irradiance. Efficacies were established for two irradiances within the aforementioned optimum irradiance range: 9.0×10^{12} W/cm^2 and 7.7×10^{12} W/cm^2. Successful OP was observed in 50 out of 92 optoperforated cells (54% efficiency) for 9.0×10^{12} W/cm^2 and in 90 out of 133 optoperforated cells (68% efficiency) for 7.7×10^{12} W/cm^2. As such, 7.7×10^{12} W/cm^2 was used for the remaining OP procedures of this work.

At this irradiance, fluorescence-bright field overlay images in Fig. 2.5, indicate that the pore formed in the cell wall is between 2 and 2.5 μm in diameter. In comparison to the laser

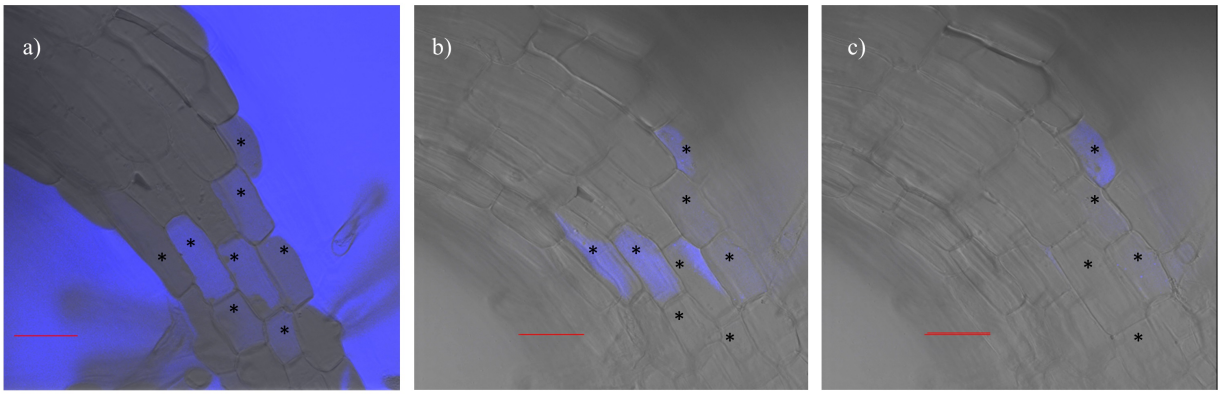

Figure 2.4: Optoperforated cells exhibiting 10 kDa dextran-cascade blue dye conjugate uptake 0.5 h post laser exposure (a), and 72 h post exposure (b, c). Panel (b) is at the 0 μm Z-plane of focus and (c) is at -14 μm. Asterisks = OP cells visible in plane. Bar = 50 μm.

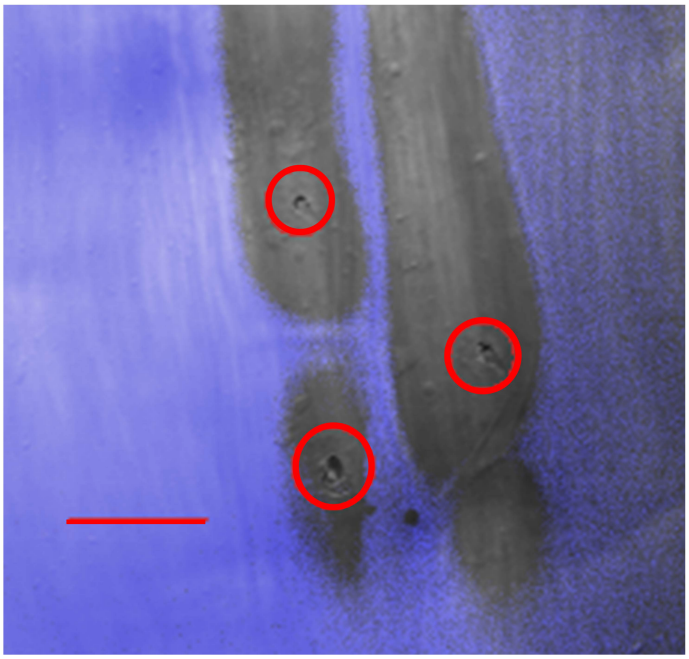

Figure 2.5: *Arabidopsis* stem epidermal cells subjected to laser optoperforation at 7.7×10^{12} W/cm^2 for 0.64 μs showed hole formation, where indicated by red circles, less than 2.5 μm in diameter. Bar = 20 μm.

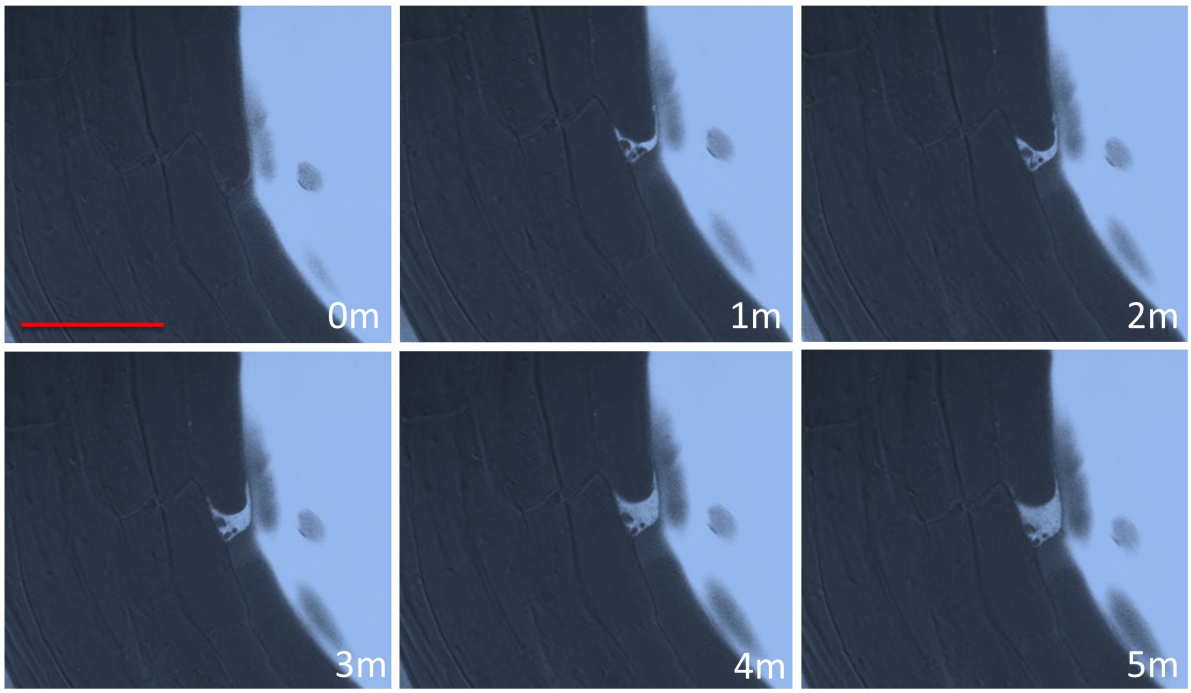

Figure 2.6: Confirmation of symplastic uptake of cascade blue dye over 5 minutes. Vacuolar membrane is visible as well as the outline of other organelles, suggesting dye is dispersed inside the plasma membrane (Media 3). Bar = 50 μm.

spot size, the observed pore dimension indicates that the laser-generated tensile stress in not confined to the focal volume at this irradiance for cell walls. The rigid nature of the cell wall constituents (cellulose, lignin), in contrast to those of the plasma membrane, may be more susceptible to these stress waves, facilitating larger pore formation.

By monitoring the temporal evolution of the fluorescent emission within a targeted cell after an optoperforation event, the observed rate of diffusive flow can indicate the time scale of the repair mechanisms for the plasma membrane. To this purpose, as shown in Fig. 2.6 and Media 3, time-lapse images were taken over a five minute period in which the OP protocol was applied to single cells of the *Arabidopsis* stem surrounded by a 10 kDa-dextran CB

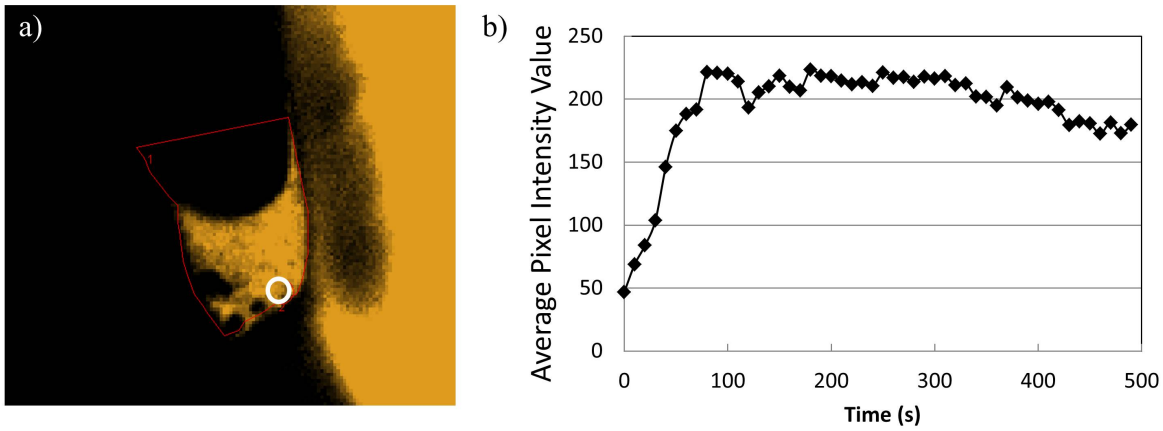

Figure 2.7: Time-resolved cascade blue conjugated dextran fluorescent intensity within optoperforated cell (a), indicating rapid influx of dye through artificial pore, and subsequent pore sealing and dye redistribution throughout cellular confines (b).

conjugate. Dye is incorporated through the cell wall and what appears to be the cytoplasm as defined by the outline of the intact vacuolar membrane and organelles that are distinct from the background. In this region, demonstrated in Fig. 2.7(a), the fluorescence emission increases monotonically for the first 90 seconds until reaching an upper limit and then, at the 300 second mark, gradually recedes from that limit as shown in Fig. 2.7(b).

The initial increase in fluorescence is indicative of a rapid influx of dye through the laser-formed pore in the cell wall and plasma membrane. Since the increase stalls at an intensity below the saturated intensity in the exogenous medium, this behavior suggests that the pore in the plasma membrane has been sealed at the onset of the upper limit. The subsequent decrease in irradiance at 300 s is a consequence of the dye diffusing within the cytoplasm and/or diffusion of unincorporated dye from the apoplast to the extracellular space.

In order to confirm that extracellular dye was incorporated into the cytoplasm and not just in the apoplastic space between cell wall and plasma membrane, cells were treated with 5 M NaCl solution to plasmolyse the cells of a seedling 24 hrs post optoperforation. As shown in

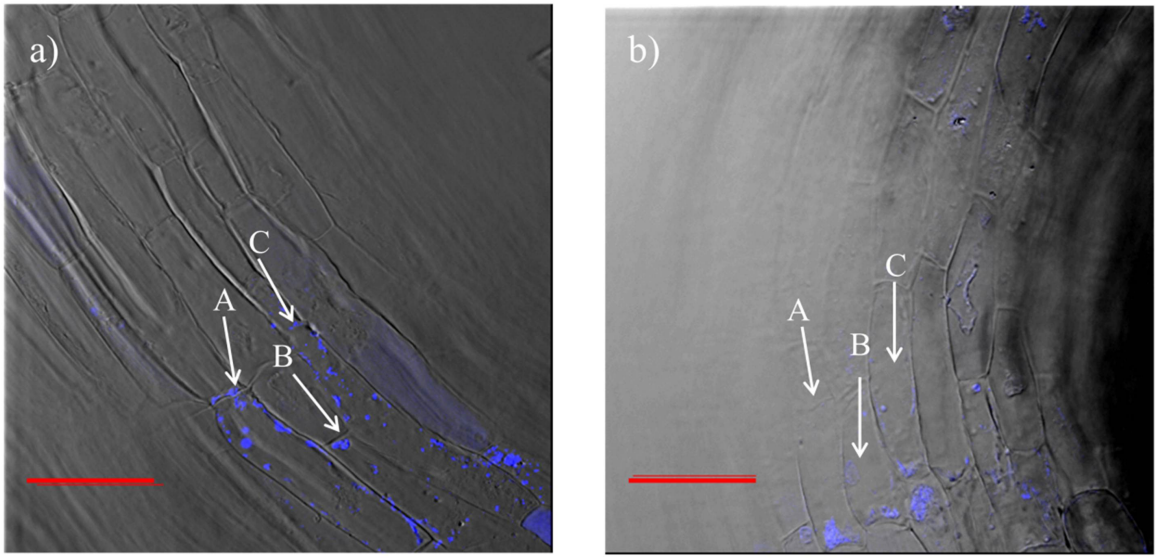

Figure 2.8: Cascade blue-10 kDa dextran appearance within cells before (a) and after (b) treatment with 5 M NaCl. The addition of saline solution changes the focal plane and orientation of the root so cells of interest are denoted by letters A, B, and C. Bar = 50 μm.

Fig. 2.8(a), prior to addition of salt solution, the dye-dextran conjugate is seen in discrete yet dispersed areas, possibly due to compartmentalization for degradation. The effect of the salt solution was rapid, so imaging was done immediately following addition of the solution. After treatment the dye aggregates, as a result of plasmolysis, the shrinking of the plasma membrane in response to osmotic stress can occur and shown in Fig. 2.8(b).

2.4 Conclusion

The formation of a transient pore within the plasma membrane of an intact plant cell is a unique accomplishment, particularly when utilizing common microscopy equipment. This work has demonstrated the efficacy of laser mediated optoperforation for pinpoint accurate targeting of cells within a plant stem for long-term symplastic retention of an extracellular dye conjugate, as confirmed by repeated imaging, presented in Fig. 2.4 and Fig. 2.5, and

saline treatment, as demonstrated in Fig. 2.8. From our observations, we conclude that the focused fs NIR laser beam creates a hole in the cell wall and allows for a temporary breach of the plasma membrane sufficient for extracellular material to be incorporated into the cell with efficacies of up to 68%. It is notable that commonplace confocal microscope setups with the addition of a fs laser source can be used for this relatively simple "point-and-shoot technique." Only minimal technical knowledge is required for a researcher to obtain similar results.

The technique presented here has multiple applications related to determining cell function and fate. Specific cells can be loaded with dyes or proteins that traffic into neighboring cells or otherwise influence function of surrounding cells. Long-lived, immobile dyes could be used as a "molecular tattoo" to mark cell fate in developing tissues over time. Ideally, the approach can be used to transform single cells with new genes or silencing constructs to investigate the role of specific cellular context in plants. Additionally, our glass-bottomed, sealed chamber is capable of accommodating OP experiments on meristem cells in the root and shoot apices which could allow for transformation of organs and the development of chimeric plants, important in the emerging field of single-cell biology.

2.5 Acknowledgements

This work was supported by NSF award IOS-0843372 to JHW, with additional support from and U.S. Department of Agriculture Hatch Project no. 135798. The authors are grateful for funding from the Institute of Critical Technology and Applied Sciences (ICTAS) at Virginia Tech, the EIGER IGERT (NSF DGE-0504196), and the lab of Dr. Jason Barone for use of TEMPO-oxidized nanocellulose material. G. A. Khodaparast would like to acknowledge the support of NSF-REU supplement as part of the NSF-Career Award DMR-0846834. We also

thank Professor Hans Robinson for his inputs.

Chapter 3

Photoluminescence lineshape and dynamics of localized excitonic transitions in InAsP epitaxial layers

T. R. Merritt, M. A. Meeker, B. A. Magill, G. A. Khodaparast*
Department of Physics, Virginia Tech, Blacksburg, VA 24061, USA

S. McGill
National High Magnetic Field Laboratory Florida, Tallahassee, FL. 32310, USA

J.G. Tischler
Naval Research Laboratory, Washington, DC 20375, USA

S. G. Choi**
National Renewable Energy Laboratory, Golden, CO 80401, USA

C. J. Palmstrøm
Department of Electrical and Computer Engineering and Materials Department, University of California, Santa Barbara, CA 93106, USA

*Author to whom correspondence should be addressed.

Keywords: Photoluminescence; III-V semiconductors; excitons and related phenomena; magneto-optical effects; magnetoexcitons; molecular, atomic, ion, and chemical beam epitaxy.

Abstract

The excitonic radiative transitions of $InAs_xP_{1-x}$ (x=0.13 and x=0.40) alloy epitaxial layers were studied through magnetic field and temperature dependent photoluminescence and time-resolved photoluminescence spectroscopy. Whereas the linewidth and lineshape of the exciton transition for x=0.13 indicate that the alloy components are homogeneously distributed, those of x=0.40 suggest the presence of localized exciton states caused by potential fluctuations due to compositional disorder. This localization is further supported by the behavior of the exciton transitions at low temperature and high magnetic fields. $InAs_{0.4}P_{0.6}$ exhibits anomalous "S-shaped" temperature behavior of the excition emission peak below 100 K as well as linewidth broadening at high magnetic fields due to the compression of the excitonic volume amid compositional fluctuations. Finally, photoluminescence decay patterns suggest that the excitons radiatively relax through two channels, a fast and a slow decay. While the lifetime of the fast decay is comparable for both compositions ($\sim$30 ps), that of the slow decay increases from 206 ps to 427 ps as x increases from 0.13 to 0.40, attributable to carrier migration between the localization states of $InAs_{0.4}P_{0.6}$.

3.1 Introduction

By altering the alloy composition, InAsP ternary alloys are capable of assuming a wide range of band gaps, spanning from 0.35 to 1.35 eV at room temperature. The ability to band gap engineer in this range is an attractive feature for a variety of optoelectronic applications, most notably for those involving modern optical telecommunication [30, 31], broadband photodetectors [32], and mid-IR lasers [33, 34]. Furthermore, InAsP alloys are capable of assuming a wide range of g-factors; this includes g=0, a desired attribute for semiconductor-

based quantum communication applications [35]. Investigating the dynamics of carriers involved in radiative transitions in these alloys not only provides a means to assess and improve sample quality, but also aids in the design and optimization of device structures. However, while the morphology and the electronic properties of InAsP have been extensively explored [36, 37, 38, 39, 40, 43, 44, 45, 46, 60], studies concerning optical characterization are limited [43, 44, 45, 46]. Although there are a large number of optical studies involving quantum structures [47, 48, 49, 31], alloy epilayers are more appropriate when considering fundamental optical transitions since confounding effects, such as quantum confinement and interface-related defects, are avoided.

The optical properties of ternary alloy systems are dominated by excitonic transitions [41] and the behavior of the linewidths associated with those transitions yield important information concerning the quality of the alloy system. For instance, of particular interest is the subject of alloy broadening, in which fluctuations in the alloy composition results in an inhomogeneously broadened excitonic energy, resulting in larger linewidths than those observed in the binary constituents of the alloy [42]. While there are a few reports on excitonic linewidths in InAsP alloys [43, 44, 45, 46], these studies do not provide a robust treatment of alloy broadening. Huang *et al.*[44] reported full width at half maximum (FWHM) linewidths at 20 K of strained-relaxed $InAs_xP_{1-x}$ alloy epitaxial layers ($0<x<0.6$), grown by MOVPE, ranged from 12-15 meV. Based on comparisons with excitonic linewidths in InP and X-ray diffraction measurements, they concluded that compositional inhomogeneity in their samples was minimal. However, a systematic optical study investigating the full character of excitonic localization was not pursued; for instance, the magnetic field and temperature dependencies were not assessed. Magnetic fields have the effect of exacerbating alloy broadening which, in turn, can reveal the extent of compositional disorder, if present [59]. In addition, the localization energy of excitons can be determined from the temperature dependence of exciton

emission energy [63].

In this work, we present experimental investigations into the optical properties of $InAs_xP_{1-x}$ (x=0.13 and x=0.40) epitaxial layers using low temperature photoluminescence (PL) measurements. Compositional disorder is assessed from linewidths of excitonic transitions at low temperatures. Furthermore, the temperature evolution of the PL spectra of these epliayers is analyzed to determine the degree of exciton localization. In addition, the effect of applied static magnetic fields on excitonic energies (diamagnetic shift) and linewidths in these alloys is determined. Finally, the excitonic recombination dynamics are discussed in the context of time-resolved PL (TRPL) measurements.

3.2 Experimental Setup

$InAs_xP_{1-x}$ epitaxial layers were prepared by chemical beam epitaxy (CBE) on Fe-doped semi-insulating InP (001) substrates. Further details concerning sample growth are available in [50]. The compositions of the alloys presented in this work, x=0.13 and x=0.40, were verified by triple-axes high resolution x-ray diffraction measurements using Vegard's rule. By means of ellipsometry, the thicknesses of the epilayers were determined to be 2.2 and 4.3 μm for x=0.13 and x=0.40, respectively. These thicknesses are well beyond the critical thickness for strain relaxation [36], as supported by x-ray reciprocal-space mapping analysis.

PL measurements were performed using an amplified Ti:Sapphire laser as the excitation source, operating at 800 nm with a pulse width of 150 fs and a repetition rate of 1 kHz. Samples were mounted in a 17.5 T superconducting magnet and PL signals were collected through a 0.6 mm core-diameter multimode fiber, delivered to a 0.75 m focal length spectrometer with a 600 grooves/mm grating, and detected by either a liquid-nitrogen-cooled charge-coupled device (CCD) or InGaAs array. All magnetic field measurements were car-

ried out using a Faraday geometry, in which the direction of the field was perpendicular to the epilayer plane and parallel to the optical excitation. TRPL measurements were performed using a synchroscan streak camera (Hamamatsu Photonics) with a temporal response of 2 ps.

PL spectra are subjected to a nonlinear damped least-squares fitting using Voigt profiles, approximated by a piecewise function involving a Taylor Expansion about precomputed points and a fifth-order Gaussian-Hermite quadrature [51]. Fitted data presented in this work yielded adjusted R^2 values greater than 0.980.

3.3 Results and Discussion

3.3.1 Lineshape analysis of excitonic transitions

Figure 3.1 shows PL spectra for $InAs_xP_{1-x}$ ternary alloy epitaxial layers measured at 5 K under an excitation fluence of 6 $\mu J/cm^2$. Both spectra involve near band edge transitions, attributable to excitonic transitions, X. The asymmetric excitonic emission for x=0.40 can seemingly be described by two Voigt profiles (see below); however, the profile on the high energy side is an artifact of the high energy tail. This tail feature is indicative of spatial fluctuations in the band gap produced by alloy disorder. Under low excitation, the characteristic time needed for carriers to migrate to lower energy sites is shorter than the radiative recombination lifetime; hence, electron-hole pairs preferentially recombine from absolute potential minima, skewing the emission toward the lower energy side [53].

The spectrum for x=0.13 also possesses an energetically lower, much broader transition. This weaker shoulder has been attributed to free to bound transitions involving a shallow acceptor [43, 44], or a donor- like defect to an acceptor level or valence band transition

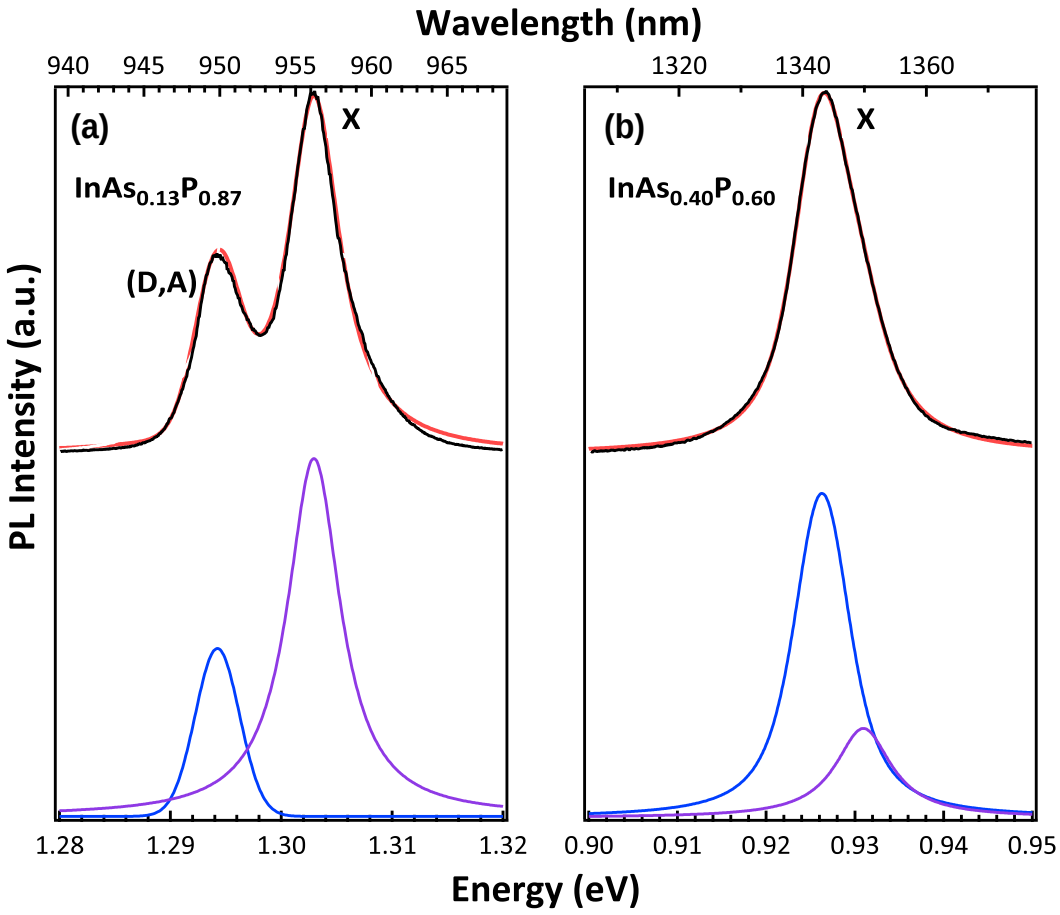

Figure 3.1: Photoluminescence spectra for $InAs_xP_{1-x}$ alloy epitaxial layers measured at 5 K with As compositions of (a) 0.13 and (b) 0.40. The fitted spectra (solid red line) overlays experimental values (black dots), and the Voigt profiles that contribute to those fitted spectra are offset below.

[46]. When increasing excitation fluence by two orders of magnitude (not shown), this lower energetic transition redshifts, supporting its classification as a donor-acceptor pair (D, A) recombination since Coulomb interaction of donors and acceptors as a function of their separation would lead to a shift in emission energy with excitation density [52].

In addition, for both compositions, the peak energy and linewidth for the energetically higher transitions did not show an appreciable dependence on excitation density, corroborating our earlier assignment that these peaks are due to excitons.

Regarding the excitonic transitions, the peak energies and FWHM linewidths at 4 K, determined from the fitting protocol, are 1.3030 eV and 5.7 meV for x=0.13, and 0.9263 eV and 7.6 meV for x=0.40. The shift of the excitonic transition toward lower energies with increasing x corresponds to the predicted band gap reduction associated with an increasing As composition. In contrast, the increase of the linewidth with x suggests the onset of alloy broadening due to compositional disorder.

Through lineshape analysis at low temperatures, the degree of alloy broadening can be assessed, ableit in a limited fashion. Typically, the lineshape of excitonic optical transitions in binary semiconductors can be approximated as Lorentzian, resulting from homogeneous lifetime broadening [53]. In contrast, random compositional disorder in alloy semiconductors incurs an inhomogeneous broadening on these transitions, producing lineshapes with a nearly Gaussian profile [53, 62]. By performing spectral decomposition of the PL with a function that is the convolution of both profiles, *i.e.* the Voigt profile, the relative contributions of the various broadening mechanisms can be inferred. The Voigt profile is given by [54],

$$\Phi(u,v) = \frac{1}{\alpha_G}\sqrt{\frac{\ln 2}{\pi}}K(u,v) \tag{3.1}$$

where $K(u,v)$, known as the "Voigt function," is given by

$$K(u,v) = \frac{v}{\pi}\int_{-\infty}^{\infty}\frac{exp(-t^2)}{v^2+(u-t)^2}dt \tag{3.2}$$

$$\text{with} \quad \begin{aligned} u &= \frac{\nu-\nu_0}{\alpha_G}\sqrt{\ln 2} \\ v &= \frac{\alpha_L}{\alpha_G}\sqrt{\ln 2} \end{aligned}$$

where α_G and α_L are the half-widths of the Gaussian and Lorentzian components, respectively, and ν-ν_0 is the distance from the profile center.

In Fig. 3.1, results of this deconvolution analysis are displaced below the observed spectra for x=0.13 and x=0.40. The Lorentzian and Gaussian contribution in each fitted peak can be determined from the shape factor, v, as defined above. According to this definition, a shape factor of zero signifies a Gaussian lineshape; as this factor increases, the Lorentzian component becomes more prominent. The shape factors for the excitonic transitions for x=0.13 and x=0.40 are 28 and 0.8, respectively, indicating that the former can be approximated as Lorentzian whereas the latter is an admixture of the two lineshapes. Since inhomogeneous broadening is a necessary attribute of alloy broadening, the shape factors indicate the possibility of modest alloy broadening in x=0.40 and the lack thereof in x=0.13.

This finding is further supported by ellipsometic and x-ray diffraction (XRD) studies of these structures [50]: The broadening parameters of second-energy-derivative of ellipsometric spectra were larger for mid-compositions ($0.4<x<0.6$) than for compositions closer to binary end-points; in addition, XRD rocking curves for x=0.40 were broader than those of x=0.13.

3.3.2 Temperature dependence of exciton luminescence

The thermal behavior of the PL spectrum is incontrovertibly affected by the distribution of alloy fluctuations within a semiconductor alloy. Fig. 3.2 shows the lattice temperature dependency of the peak position of the dominant exciton transition for both compositions considered, where these peak positions were determined from the aforementioned fitting protocol. At high temperatures (>100 K), both compositions experience a redshift in peak position with increasing temperature, attributable to the temperature dependence of the band gap, $E_g(T)$. With regard to this thermal dependency, the phonon coupling model proposed by O'Donnell and Chen [55] is more appropriate for describing $E_g(T)$ for $InAs_xP_{x-1}$ alloys than either the Varshini or Bose-Einstein equations [56]. This model asserts that the

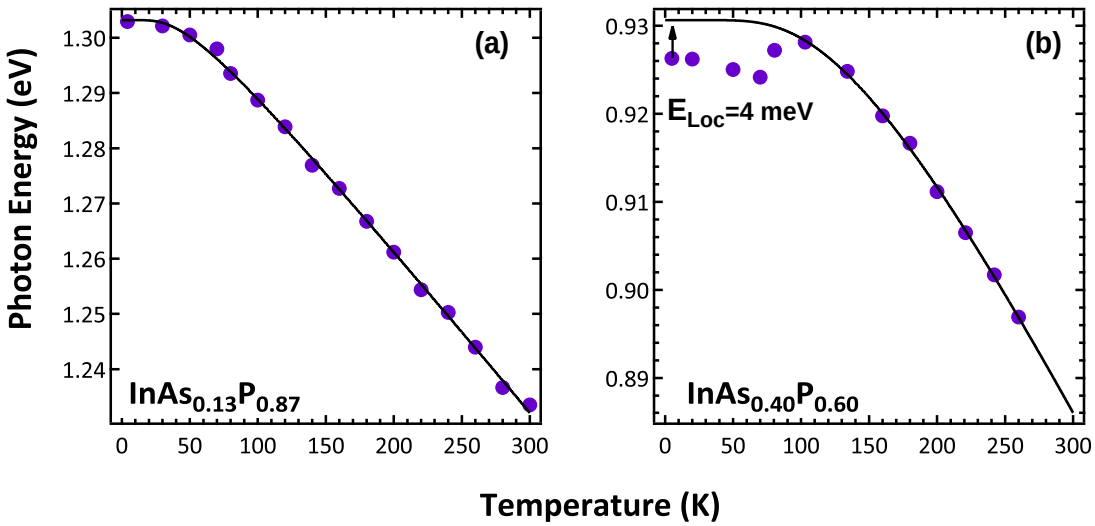

Figure 3.2: Temperature dependency of the dominant PL emission peak of $InAs_xP_{1-x}$ for (a) x=0.13 and (b) x=0.40. Solid circles indicate measured values whereas the solid lines denote the best fit of Eq. 3.3 to the high temperature measurements (>100 K).

temperature dependence of the band gap is as follows:

$$E_g(T) = E_g(0) - S\langle h\omega\rangle[\coth(\langle h\omega\rangle/2kT) - 1] \tag{3.3}$$

where S is a dimensional coupling constant and $\langle h\omega\rangle$ is the average phonon energy.

The solid lines in Fig. 3.2 for x=0.13 and x=0.40 represent the nonlinear least squares fit of Eq. 3.3 with the excitonic peak positions for T>100 K; values of the best fit parameters are given in Table 3.1.

While the thermal behavior of the excitonic peak position for x=0.13 follows closely with that of the band gap well into the low temperature regime, the peak position for x=0.40 exhibits a markedly different behavior below 100 K. In fact, this divergence from the band gap behavior is known as the thermal S-shape emission shift prototypical of semiconductor alloy systems with inhomogeneously distributed alloy potential fluctuations [57]. This behavior features

As concentration (%)	$E_g(0)$ (eV)	S	$\langle h\omega \rangle$ (meV)
13	1.303	1.73	11.4
40	0.930	1.89	36.3

Table 3.1: Best fit parameters for the high temperature dependence of the dominant PL emission peak for $InAs_xP_{1-x}$.

a red-blue-red shift of the excitonic peak positions with increasing temperature caused by thermal migration of excitons from localized to delocalized states. The initial redshift occurs when excitons are supplied with sufficient thermal energy to overcome local potential barriers, which allows the excitons to relax into absolute minima. Increasing the lattice temperature further results in the thermal excitation of the excitons into energetically higher extended states; hence, the peaks become blueshifted. At large enough temperatures, ample thermal energy prevents the localization of excitons, at which point any further temperature increase engenders a second redshift in peak positions due to band gap reduction. In other words, the S-shape feature that is present in the peak position temperature dependence for x=0.40 (Fig. 3.2) is due to a competitive process between localized and delocalized excitonic states and the existence of these localized states are a result of alloy disorder.

Furthermore, at the lowest measurement temperature, the deviation of the peak position from the expected band gap behavior given by Eq 3.3 describes the localization energy [63]. At 5 K, E_{Loc} is approximately 4 meV for x=0.40, as indicated in Fig. 3.2.

3.3.3 Diamagnetic shifts and magnetic broadening

Behavior of these excitonic transitions in the presence of a magnetic field can also indicate the extent of the compositional disorder. Fig. 3.3 shows the evolution of the PL spectra as a

function of magnetic field strength for both $InAs_xP_{1-x}$ compositions. Upon the application of a magnetic field, the peak position of the excitonic emission, X, for x=0.13 and x=0.40 experiences a blue shift; in addition, for x=0.13, the impurity transition (D, A) rapidly subsides and the peak position shifts to higher energies.

An explanation for this latter behavior is that, as the magnetic field is increased, the wavefunctions of the localized, impurity states shrink and, as a result, the wavefunction overlap between the states involved in this transition is reduced, thereby, diminishing its oscillator strength. Furthermore, the binding energy of the impurity states decreases at higher fields, prompting a reduction in the number of ionized states at low temperatures; in turn, this both diminishes the peak intensity of and incurs an energetic shift in the impurity transition.

With regard to the excitonic behavior, the excitons undergo a diamagnetic shift as a result of Landau quantization [58], resulting in their shift to higher energies. In addition, the linewidth is expected to increase in disordered alloys. This behavior is due to the compression of the excitonic wavefunction under an increasing magnetic field, which causes the lineshape to be more susceptible to the local potential fluctuations resulting from compositional disorder [62]. In turn, this results in a magnetic broadening of the linewidths. While many groups have proposed models to describe the magnetic field dependency of these quantities, we prescribe to the formalism of Mena *et al.* and Lee *et al.* [62, 59].

Both employ the same Hamiltonian to describe an exciton in a static magnetic field directed along the z-axis, relying on the symmetric gauge and cylindrical coordinates:

$$H = -\nabla^2 + \frac{\gamma}{i}\frac{\partial}{\partial\phi} + \frac{1}{4}\gamma^2\rho^2 - \sqrt{\frac{4}{(\rho^2 + z^2)}} \tag{3.4}$$

such that lengths and energies are taken in units of the excitonic radius, $a_{ex} = \epsilon\hbar^2/\mu e^2$, and the effective Rydberg, $R = \hbar^2/2\mu a_{ex}^2$, respectively, where ε is the dielectric constant of

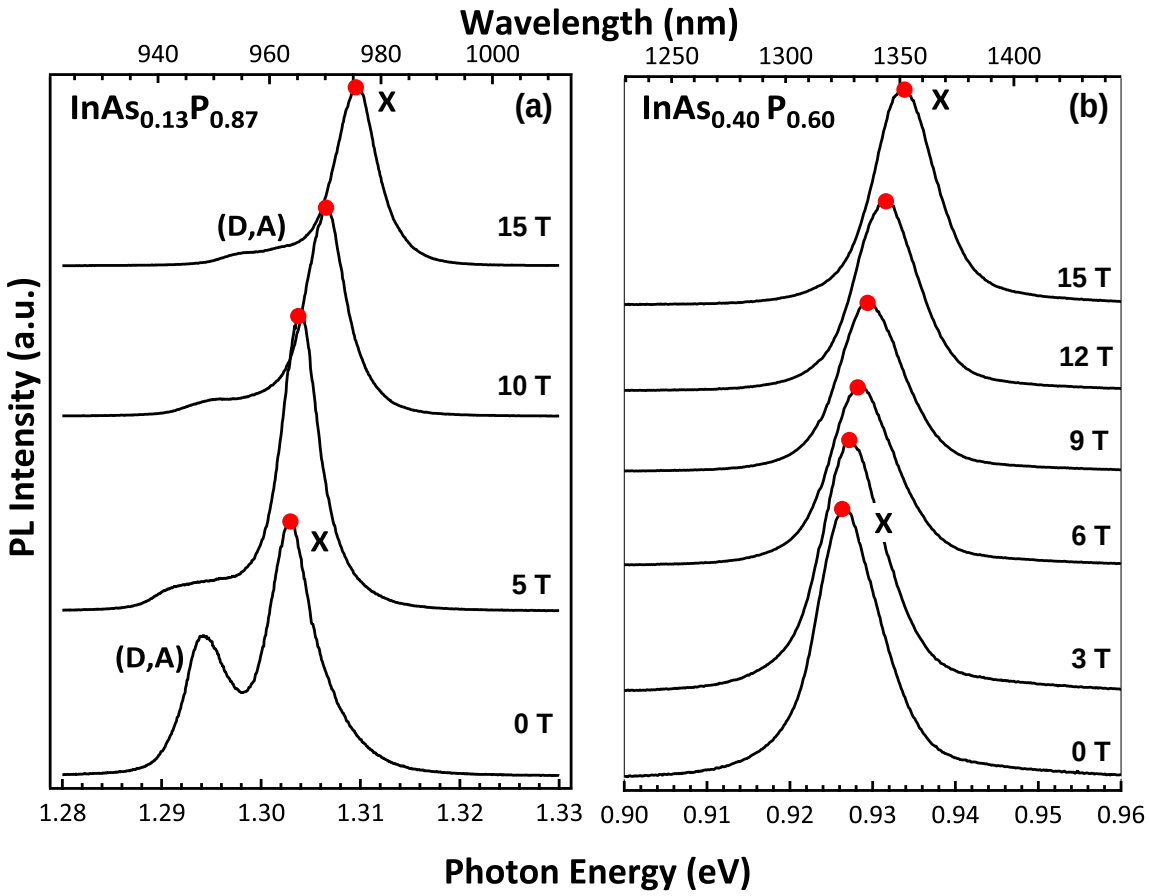

Figure 3.3: Magnetic field dependency of the PL spectra for $InAs_xP_{1-x}$ for (a) x=0.13 and (b) x=0.40. The emission peak position (solid circles) for both compositions experience a blueshift with increasing magnetic field strength, which is characteristic of a diamagnetic shift. All spectra are normalized and vertically shifted for clarity.

the alloy and μ is the excitonic reduced mass. The diamagnetic term, $\gamma^2\rho^2/4$, contains the dimensionless parameter γ, which is a measure of the magnetic field strength, defined as $\gamma = \hbar eB/2R\mu c$. The grounds state wavefunction for the Hamiltonian, Eq.3.4, was determined through variational calculations using the trial wavefunction

$$\Psi(\rho, z) = A \exp[-\lambda_1\sqrt{\rho^2 + z^2} - \lambda_2\rho^2 + \lambda_3 z^2] \tag{3.5}$$

where A is the normalization constant, and λ_1, λ_2, and λ_3 are the variational parameters

whose values are those that minimize $\langle H \rangle$.

To model the magnetic broadening, the calculations of Mena rely on the expectation value of the excitonic volume; in contrast, Lee [62] relies on a quantum statistical approach. Their derived expressions for linewidths due to compositional variation can be generalized as such,

$$\sigma(x) = 2\sqrt{(2\ln 2\ (\frac{\partial E_g(x)}{\partial x})^2\ \Omega(\Psi))} \tag{3.6}$$

where $\partial E_g(x)/\partial x$ describes the variation of the direct band gap energy with respect to alloy composition and $\Omega(\Psi)$ is a broadening function that contains the magnetic field dependency. This function assumes the following form:

$$\Omega_{Mena} = \frac{V_c}{a_{ex}^3}(\frac{4\pi}{3}\langle\Psi|(\rho^2+z^2)^{\frac{3}{2}}|\Psi\rangle)^{-1} \tag{3.7}$$

$$\Omega_{Lee} = (\frac{V_c}{a_{ex}^3})^2 \sum_{k=-\infty}^{\infty}\sum_{j=1}^{\infty}(2j+1)|\Psi(j\Delta\rho, k\Delta z)|^4 \tag{3.8}$$

where a is the lattice constant, V_c is the primitive cell volume, and $\Delta\rho$ and Δz are dimensional increments depending on the crystalline structure. For zinc blends, $V_c{=}a^3/4$, $\Delta\rho{=}a/\sqrt{2\pi}a_{ex}$, and $\Delta z{=}a/2a_{ex}$. To calculate $\sigma(x)$ in $InAs_xP_{1-x}$, physical values from Ref. 50 and Ref. 60 were used. Linear interpolation between the properties of InP and InAs was employed to determine the dielectric and lattice constants:

$$\epsilon(x) = 12.5(1-x) + 15.2x \tag{3.9}$$

$$a(x) = 5.87(1-x) + 6.06x \text{ Å} \tag{3.10}$$

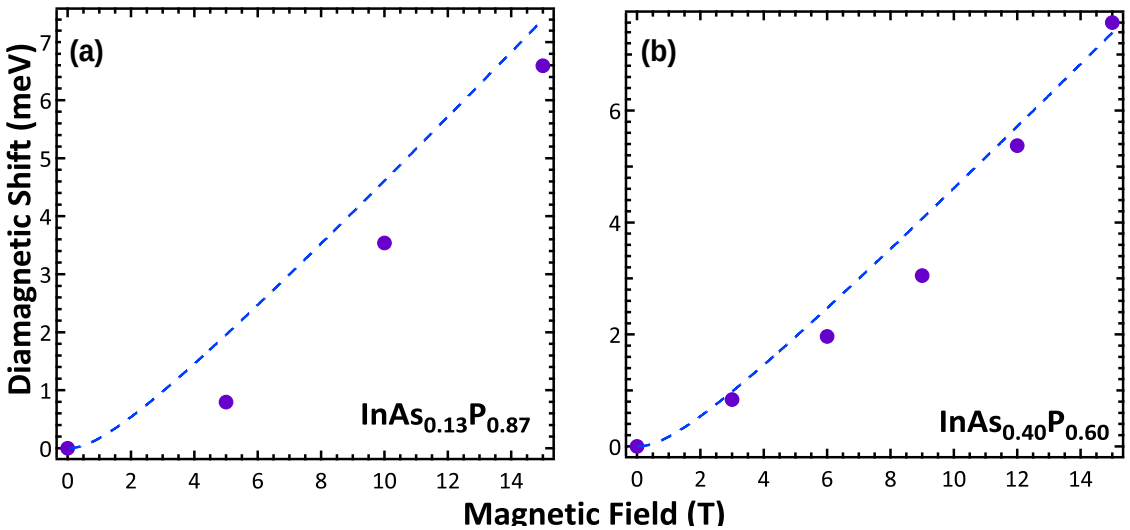

Figure 3.4: Variation of the diamagnetic shift of the excitonic transition as a function of magnetic field in $InAs_xP_{1-x}$ for (a) x=0.13 and (b) $x = 0.40$. Experimental values (solid circles) were measured at 5K and fitted (dashed curve) to pre-tabulated values of $\langle\gamma^2\rho^2/4\rangle$ to determine excitonic reduced masses. For x=0.13 and $x = 0.40$, those reduced masses were determined to be $0.051m_0$ and $0.048m_0$, respectively.

The variation of the band gap energy, $\partial E_g(x)/\partial x$, at 4 K in eV is given by:

$$\frac{\partial E_g(x)}{\partial x} = -1.09 + 2.4x \tag{3.11}$$

Reduced masses were determined experimentally from the diamagnetic shifts exhibited by both compositions. These observed shifts of the peak position with magnetic field were least-squares fit to precomputed curves calculated from the expectation value of the diamagnetic term. Fig. 3.4 displays the results of this fitting procedure (dashed line) alongside the measured values (solid circles). From the fitted curves, the reduced masses of the excitons in the plane perpendicular to the magnetic field were determined to be $0.048m_0$ and $0.051m_0$ for x=0.40 and x=0.13, respectively, where m_0 is the electron mass in free space.

Figure 3.5 displays the linewidths as a function of magnetic field for the calculated values, solid (Mena) and dashed (Lee) lines, along with the experimental values (solid circles). The

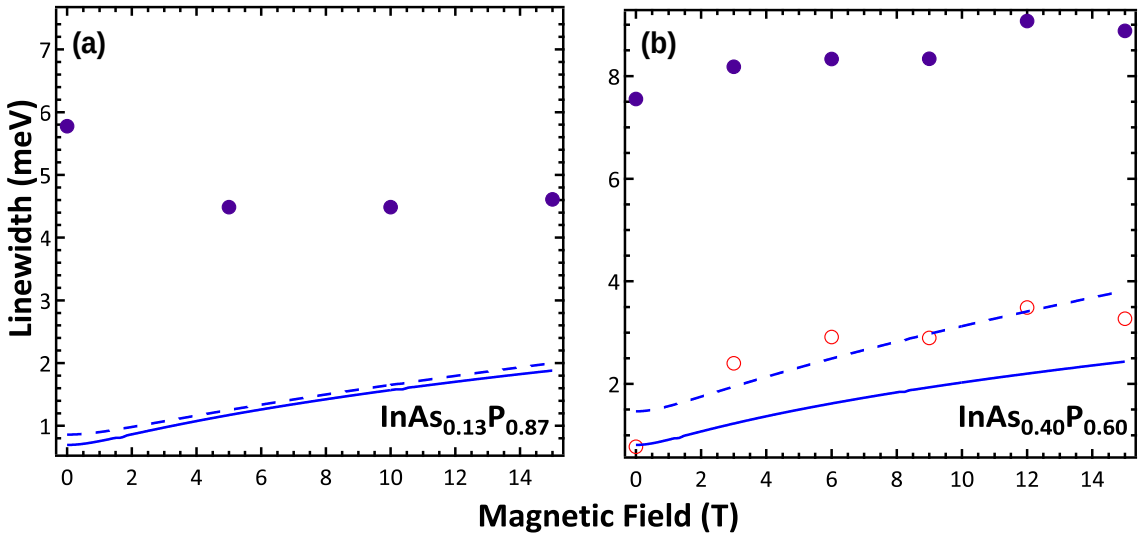

Figure 3.5: Variation in the excitonic linewidth for $InAs_xP_{1-x}$ alloy epitaxial layers as a function of magnetic field for As compositions of (a) 0.13 and (b) 0.40. Excitonic linewidths determined from the line shape analysis are represented by solid circles. The dashed and solid lines were produced from the theoretical calculations of alloy broadening on excitonic linewidths according to the derivations of Lee *et al.* and Mena *et al.*, respectively. For Fig. (b), the open circles are the result of offsetting the measured values (solid circles) of x=0.40 by those of x=0.13.

magnetic field dependency of the excitonic linewidth for x=0.13 clearly diverges from the expected behavior for alloys with compositional disorder. In fact, the reduction of linewidth with an increasing magnetic field is indicative of ordered alloys, where such a behavior is attributed to a diminished exciton-impurity scattering cross section at high magnetic fields [61].

In contrast, the linewidth for x=0.40 steadily increases with B, albeit displaced from the predicted values by approximately 6 meV. However, the considered models only account for inhomogeneous linewidth broadening due to compositional disorder and, hence, do not include homogeneous contributions, which are always present at finite temperatures. To resolve the inhomogeneous contribution, we rely on the fact that the lineshape of x=0.13 is ostensively devoid of alloy broadening. As such, the homogenous contribution from the

total linewidth of x=0.40 is approximately removed from the total linewidth by subtracting the linewidth of x=0.13 at zero field from those of x=0.40. As a result, the magnetic field behavior of the modified x=0.40 linewidths (open circles) corresponds more closely with the modeled behavior described by Lee *et al.*[62]. However, in addition to compositional variation, the inhomogeneous broadening may be attributable to other broadening mechanisms, such as clustering of alloy components and Stark effects from ionized impurities. These other mechanisms may account for the deviation that still persists between measured values and the modeled behavior [62].

3.3.4 Time-resolved photoluminescence

In order to study the radiative dynamics of the exciton transitions, TRPL spectroscopy was employed. Figure 3.6 shows the temporal response of the PL spectra as a function of temperature for (a) x=0.13 and (b) x=0.40. The TRPL spectra for both compositions feature a slow and fast decay component. To determine the time scales of these radiative relaxations, the decaying portion of the temporal data was fitted (solid line) to the convolution of the instrument response function and a double-exponential decay function, with the latter being expressed as:

$$I(t) = A\ \exp[\frac{-t}{\tau_1}] + B\ \exp[\frac{-t}{\tau_2}] \tag{3.12}$$

where τ_1 and τ_2 are time constants for two decay components, and A and B are their relative contributions to the PL intensity. At zero T and 5 K, τ_1 and τ_2 were 27 and 206 ps for x=0.13, and 28 and 427 ps for x=0.40.

The source of the fast decay component is speculative, but may be due to rapid relaxation of

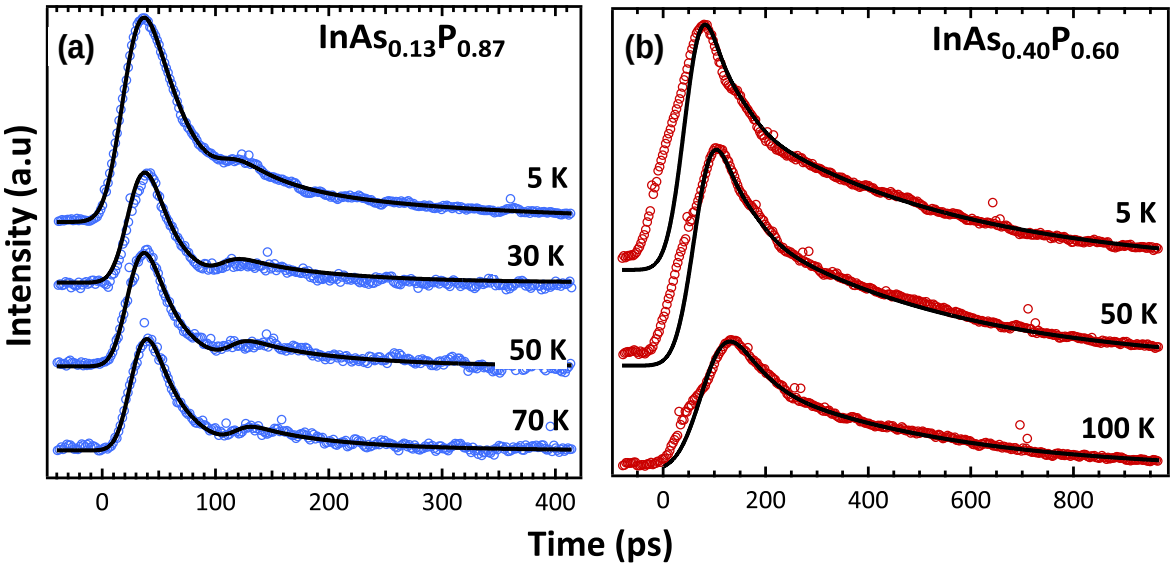

Figure 3.6: Temperature-dependent time-resolved PL spectra of $InAs_xP_{1-x}$ for (a) x=0.13 (left) and (b) x=0.40 (right). The decaying portions of the spectra (open circles) were fitted to the convolution of the instrument response function and a double exponential decay function, given in Eq. 3.12.

electron-hole pairs through nonradiative pathways, such as surface recombination or Auger cooling. In contrast, the slow decay is most likely the result of a prolonged multistep relaxation process involving carrier cooling through LO-phonon emission and, in the presence of alloy disorder, nonradiative relaxation to energetically low localization states. Due to the low excitation intensities used, cooling excitons give rise to relatively small changes in the LO phonon occupation number such that hot phonon bottlenecking is unlikely [39]. In addition, this carrier migration between localized states may account for the long rise times in the x=0.40 TRPL spectra, depicted by the initial divergence from the fitted behavior [64, 65].

Furthermore, the relaxation of cool exctions may also have to contend with localized states brought about by compositional disorder, which can conceivably account for the two-fold increase in τ_2 for x=0.40 with respect to that for x=0.13. This assertion is based on the fact that localization is analogous to impurity-related binding of excitons and the radiative

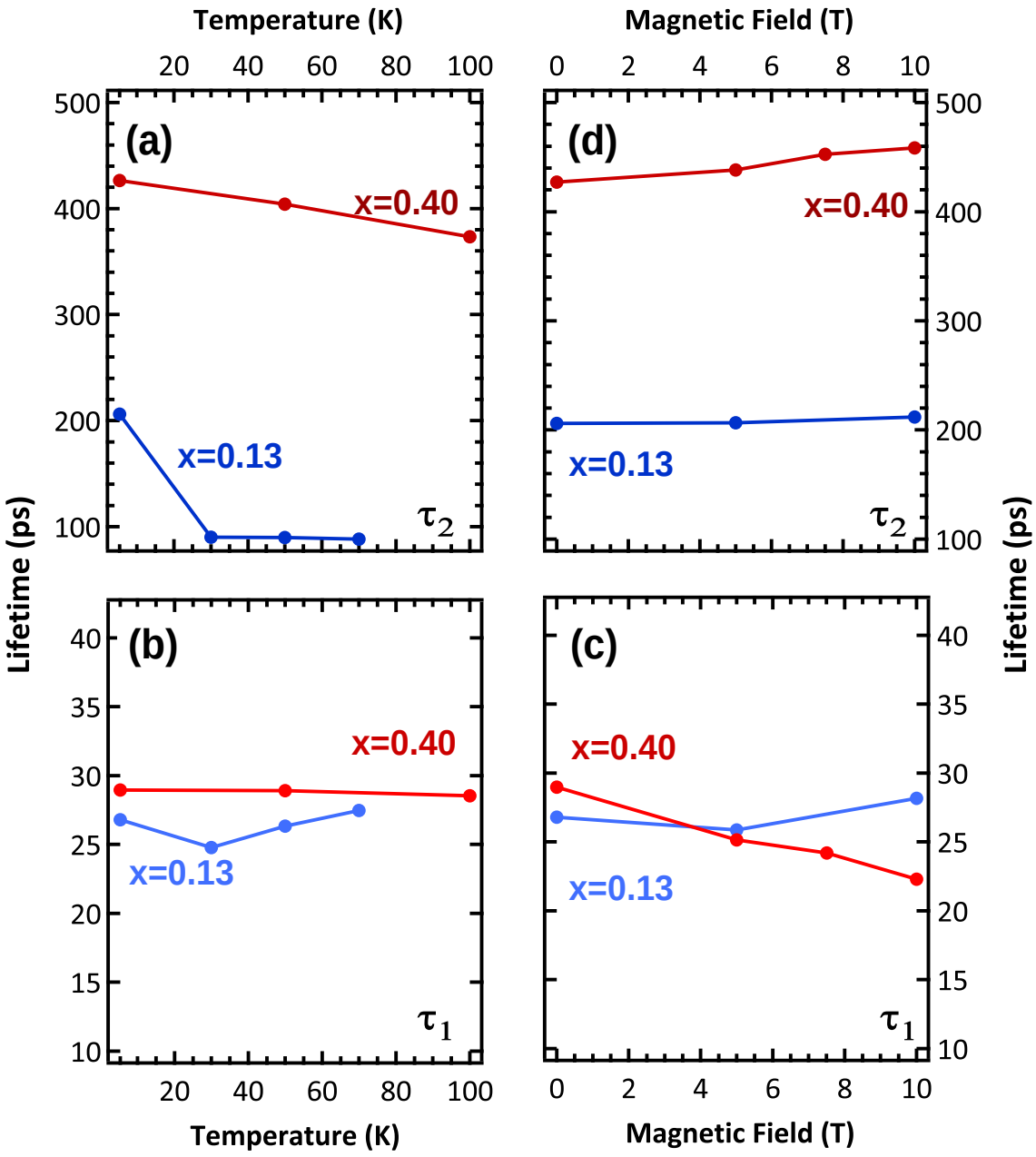

Figure 3.7: Temperature ((a) and (b)) and magnetic field ((c) and (d)) dependencies of τ_1 and τ_2, the fast and slow lifetimes of the $InAs_xP_{1-x}$ photoluminescence for x=0.13 and x=0.40. (Starting from the top left corner and proceeding counterclockwise: (a) temperature tempendence of τ_2, (b) temperature tempendence of τ_1, magnetic field tempendence of τ_1, and (d) magnetic field tempendence of τ_2.)

lifetime of bound excitons increases with binding energy [63].

This lifetime inflation due to excitonic localization also has a discernible presence in the magnetic field dependency of the TRPL. As mentioned previously, magnetic confinement acts to exacerbate the localization of excitons, which would, in turn, act to increase radiative lifetimes. The right portion of Fig. 3.7 depicts the dependence of τ_2 on magnetic field strength for x=0.13 and x=0.40, respectively. While τ_2 for x=0.13 remains largely unchanged for B <10 T, the lifetimes for x=0.40 display a noticeable dependence on B, where τ_2 increases from 427 to 459 ps as B increases from 0 to 10 T.

While the lifetimes of the fast decay for both compositions remain relatively unchanged with temperature, the slow decay lifetimes for both x=0.13 and x=0.40 exhibit a marked decrease with increasing temperature, as depicted in the left portion of Fig. 3.7. Specifically, as the lattice temperature is increased from 5 K to 100 K, τ_2 reduces from 206 to 88 ps for x=0.13, and 427 to 374 ps for x=0.40. This reduction in lifetimes is tenably attributable to the stronger influence of nonradiative recombination processes and the thermalization of localized states.

3.4 Conclusions

In summary, the excitonic radiative transitions of $InAs_xP_{1-x}$ (x=0.13 and x=0.40) alloy epitaxial layers were studied through magnetic field and temperature dependent photoluminescence and time-resolved PL spectroscopy. While the linewidth and lineshape of the exciton transition for x=0.13 indicate that the alloy components are homogeneously distributed, those of x=0.40 suggest the presence of localized exciton states caused by compositional fluctuations. The behavior of the exciton transitions for x=0.40 at low temperatures and high magnetic fields further corroborate this assertion. Below 100 K, the excition emission

peak diverges from the band gap thermal behavior, exhibiting the anomalous "S-shaped" behavior associated with alloy systems possessing exciton localization. From this divergence, the localization energy was determined to be approximately 4 meV. Under high magnetic fields, the inhomogeneous portion of the x=0.40 linewidth follows the broadening behavior expected for compressed excitonic wavefunctions in the presence of alloy disorder. Finally, the TRPL spectra feature two decay channels for the excitonic radiative transitions. While the lifetime of the fast decay is comparable for both compositions ($\sim$30 ps), that of the slow decay increases from 206 ps to 427 ps as x increases from 0.13 to 0.40, attributable to carrier migration between localization states of x=0.40.

3.5 Acknowledgments

Supported by: NSF-Career Award DMR-0846834, and by the National High Magnetic Field Laboratory through a UCGP. G. A. Khodaparast thanks the inputs from professor Alexey Belyanin and the funding from the Institute of Critical Technology and Applied Sciences (ICTAS) at Virginia Tech. ** The samples studied in this work were grown and characterized as part of S. G. Choi's PhD work at the University of Minnesota.

Chapter 4

Metal-Enhanced Upconversion of $NaYF_4$:Yb,Er Nanocrystals with Doubly Concentric Bimetallic Nanosurfaces.

T. R. Merritt[1] and G. A. Khodaparast
Department of Physics, Virginia Tech, Blacksburg, VA 24061, USA

D.L. Inglefield[1] and T.E. Long
Department of Chemistry, Virginia Tech, Blacksburg, VA 24061, USA

[1]These authors contributed equally to this work.

Keywords: nanocolloid; upconversion; nanophosphor; plasmonically enhanced emission; metal-enhanced absorption; lanthanide; interdisciplinary.

Abstract

Lanthanide-doped upconverting nanoparticles (UCNP) have the ability to convert low energy photons into high energy photons, making this material appealing to variety of scientific pursuits, from solar energy conversion to bioimaging. However, unlike their bulk equivalents, these nanoparticles are plagued by low upconversion efficiencies which limit their applicability. In order to overcome this particular disadvantage, the luminescence yield of UCNP can be increased by coupling these nanoparticles to metallic surfaces through a process known as metal-enhanced fluorescence (MEF). To this end, we present a preliminary study regarding the integration of upconverting $NaYF_4$:Yb,Er nanocrystals and concentric bimetallic nanosurfaces into a unitary nanocomposite. Precursors for these nanocomposites, bare UCNP and silica capped UCNP, are synthesized and subjected to structural and spectral analysis. While both nanoparticles produce the expected upconverted photoluminescence, the addition of a thick silica capping layer results in the redistribution of the primary emission bands in favor of the red emission, a possible consequence of interface defects between the host matrix and the amorphous silica layer. In addition, extinction efficiencies are calculated for two proposed nanocomposites that rely on Au-Ag bimetallic doubly concentric surfaces for MEF. The geometrical parameters of these nanocomposites are chosen to produce plasmonic properties necessary for the metal-induced enhancement of both the excitation and emission aspects of the upconversion process. This contrasts with previous studies of MEF in UCNP which rely on metallic structures that enhance only one of these aspects.

4.1 Introduction

Anti-Stokes emission processes, where high-energy photons are generated from low-energy pump photons, have attracted a great deal of attention due to their inherent importance and applicability to diverse research fields, including those involving solid state lasers [66, 67, 68], optical storage [69], near infrared quantum counters[66], photovoltaics [70, 71, 72], bioimaging and biotherapeutics [73, 74, 75, 102, 77]. For instance, this energy upconversion process has been used for harvesting subbandgap photons to improve solar cell conversion efficiencies [70, 72]; in addition, upconversion can be utilized in contrast agents for advanced biological labeling and imaging applications due to autofluorescence avoidance and deep detection ranges in biological tissues [74], both of which are a direct result of the near-infrared excitation spectra and large anti-Stokes shifts of these materials [75].

While various anti-Stokes mechanisms exist (Fig. 4.1), such as the widely employed processes of simultaneous two photon absorption (TPA) and second harmonic generation (SHG), upconversion based on energy transfer conversion (ETU) stands as an appealing alternative for the generation of anti-Stokes emissions [66, 78, 79]. The former processes generate upconverted emissions through virtual intermediate excited states, a mechanism reliant on high-density excitation, a requirement typically fulfilled by ultrafast lasers [78, 79]. In contrast, ETU involves non-radiative Forster energy transfer between real, long-lived intermediate excited states of neighboring luminescent ions; as a result, the requirement of high-density excitation is largely waived for ETU and, as a consequence, high conversion efficiency is allowed without the need for intense coherent excitation sources [78, 79].

In particular, lanthanide doped glasses are attractive ETU systems due to their ability to possess emissions that span the entire visible region; this feature is achieved through the judicious choice of the activator ion [79, 80]. The most efficient species of these upconversion

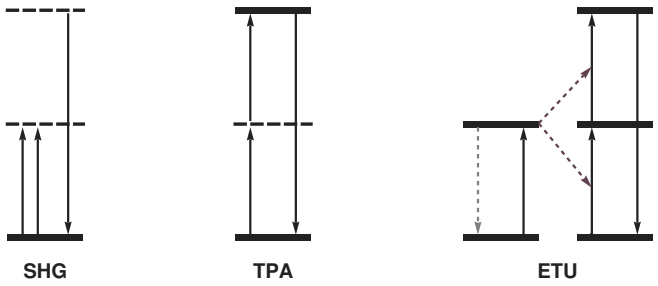

Figure 4.1: Simplified depictions of selected anti-Stokes processes. For SHG and TPA schemes, excitation is achieved through virtual states; the former generally involves excitation to a virtual upper state while the latter involves excitation to a real upper state through an intermediate virtual state. The ETU scheme relies on energy transfers between neighboring ions where the excitation energy of the sensitizer ion is successively transferred to the activator ion.

materials are fluoride glasses co-doped with the sensitizer-activator pair of Yb^{3+} and Er^{3+}, namely hexagonal $NaYF_4$:Yb,Er [81], which exhibits/enjoys upconversion quantum yields of up to 5%. This maximal quantum yield is attributable to the high absorption cross section of Yb^{3+} and the spectral overlap of Yb^{3+} 's solitary optical transition with the $^4I_{15/2} \rightarrow {}^4I_{11/2}$ transition of erbium, as well as the low optical phonon energies of hexagonal $NaYF_4$ which results in the considerable suppression of multiphonon relaxation processes [66, 81, 82].

The applicability of these materials can be further expanded by encapsulating this upconversion feature into nanoscale structures, plausibly impacting, among others, the fields of nanophotonics [83] and molecular bioimaging [73, 84]. However, unlike their bulk equivalents, $NaYF_4$:Yb,Er nanocrystals suffer from dismally low upconversion quantum yields (<1%) [77, 85]; for instance, 0.1% has been reported for 30-nm-diameter particles [85]. While already having to contend with inherently low overall absorption cross sections due to the parity forbidden 4f transitions of the erbium dopants [85, 86], nanoscale miniaturization introduces a considerable amount of surface quenching due to large surface/volume ratios [87]. This brand of luminescence quenching arises from defects and disorders caused by abrupt interruptions of lattice periodicity over a large surface area. In addition, this quenching can

originate from unsaturated bonds at the surface that render the nanoparticles susceptible to adsorbing light ions and free radicals. Both of these effects promote deleterious trap-assisted recombination, resulting in high nonradiative losses and, hence, low quantum efficiencies [87].

In order to alleviate these low efficiencies and thereby increase fluorescent yields, various approaches have been entertained. To achieve higher electronic transition probabilities of the lanthanide activators, the host lattice can be altered through substitutional doping to modify sensitizer-activator proximity in order to increase the rate of energy transfer between the lanthanide dopants [88]. In addition, modifications to local crystal fields can loosen electric dipole selection rules in high symmetry hosts, resulting in larger optical strengths [89]. With regard to the issue of surface quenching, dielectric surface coatings, typically silica shells, have been used to inhibit surface trapping by increasing the distance between luminescent ions and surface quenching centers [87]. In recent years, there has been burgeoning research interest in combining this surface capping approach with metal plasmonic surfaces to improve the optical performance UCNPs through a technique known as metal-enhanced fluorescence (MEF).

4.2 Metal-Enhanced Upconversion

In MEF schemes, the photoluminescence of a fluorophore is enhanced by vicinal metal nanostructures through resonant interactions with excited surface plasmons [90, 91], quasi-particles representing the forced, coherent oscillations of conduction electrons induced by incident radiation that are confined to the surface of the metal. This enhancement is driven by two primary mechanisms: (1) an increased excitation flux caused by enhanced local fields associated with plasmonic resonance, and (2) an increase in emission rates, signified by a reduction

in the radiative lifetimes and enhanced quantum yields [90]. The underlying cause of this latter mechanism is a point of contention. The widely disseminated and purported reason for this enhancement is due to the emissions of the fluorophore coupling with the surface plasmon modes which, through changes in the photonic density, modifies both the intrinsic radiative and non-radiative rates of the emitter in such a way as to produce higher quantum yields [91]. However, a more recent explanation for the improved quantum yields is that excited fluorophores nonradiatively transfer energy to the surface plasmon modes and, in turn, the surface plamsons radiate a replicated emission of the fluorophore to the far field, i.e. radiate the coupled quanta [92, 93]. Regardless of underlying cause, a reduced lifetime remains a distinguishing feature of MEF.

Both mechanisms of MEF have a strong spectral dependence insofar that in order for a significant enhancement to occur, a considerable overlap needs to exist between the surface plasmon resonance (SPR) scattering spectra with either the absorption or emission spectrum of the fluorophore [90, 91]. The extinction spectrum for a particular metal nanostructure is the combination of both the SPR scattering and absorption spectra; these latter spectra indicate the degree in which incident radiation of a given wavelength is dispersed or dampened, respectively [95, 94]. Furthermore, the fluorescence promotion of MEF is primarily due to the scattering component of the SPR band [95, 94]; conversely, metal-induced fluorescence quenching, which can occur due to plasmon energy dissipation, is associated with the absorption component of the SPR band [96]. Consequently, plasmonic enhancement of the excitation and emission rates relies on the degree of spectral overlap of the plasmonic scattering spectrum with either the absorption or emission spectrum of a given fluorophore, respectively.

The resonant plasma modes, along with their relative scattering and absorption behavior, are determined and thereby controlled by the composition, geometry and dimensions of the

metallic nanostructures [97]. Hence, through architectural considerations, the SPR of these nanostructures can be tailored to the optical response of a given fluorphore to, thereby, optimally promote its photoluminescence.

In addition to the spectral dependence of MEF, this phenomenon is also sensitive to the distal distance between the fluorophore and the plasmonic surface [94]. Quenching predominately occurs if the fluorophore is in direct contact with the metallic surface [98, 99, 102]. As a separation is introduced between the two bodies, typically achieved by a dielectric or molecular spacer, a critical distance emerges in which the fluorescence enhancement is maximal [77, 100]. This optimal distance arises from the distance dependencies of and the resulting interplay between the MEF mechanisms and nonradiating plasmon absorption [100]. At short distances (<5nm) dissipation of energy transferred nonradiatively from excited fluorophores to the plasmon absorption modes supersedes the gains in excitation flux produced by enhanced local fields [99]. As the distal distance increases, the efficiency of forester energy transfer drops off more rapidly than the near-field enhancement, eventually giving rise to an opportune distal distance in which MEF mechanisms preeminently dominate [94, 100]. This overall distance dependence is due to the fact that the former and latter mechanisms are inversely proportional to d^6 and d^3, respectively, where d is the thickness of the spacer [94, 96, 90]. Hence, the thickness of interceding spacers can effectively modulate the fluorescence enhancement.

Numerous studies have been reported that apply the concept of MEF to UNCP, employing a variety of metallic nanostructures to achieve luminescence enhancement, including large surface area structures [82, 99], metal islands [94, 101], and various metallic nanoparticle morphologies, including spheres [95, 102, 104, 98], rods [104, 105], and shells [77, 106, 107, 98, 108, 103, 109]. In recent years, UCNP have been incorporated into core-shell nancomposites in which the $NaYF_4$:Yb,Er nanoycrystals have been encased in concentric dielectric

and metallic nanoshells [77, 103, 109]. This architecture is particularly attractive due to this heterointegration of mulitfunctional components into a unitary nanocomposite, which is particularly apt for applications requiring colloidal particles. The incorporation of the dielectric shell encourages suppression of surface quenching centers while providing optimal distal spacing. Regarding the metallic shells, the SPR extinction spectrum, along with its scattering and absorption components, can be modified by merely adjusting the inner and outer radii of the shell without significantly altering the dimensions of the nanocomposite [97]; in addition, peripheral metallic shells provide long-term stability and can further improve biocompatibility of the enclosed UCNP [97].

Previous works featuring this core-shell architecture typically rely on a UCNP core encased in a single layer of a dielectric spacer followed by a solitary noble metal nanoshell [77, 103, 109]. In these works, the shell geometry is altered so that the extinction spectrum overlaps with either the emission or absorption spectra of the UCNP, and the thickness of the spacer is adjusted to the maximize metal-induced enhancement of the photoluminescence. For instance, Priyam *et. al* [77] developed a nanocomposite featuring a 30-nm-in-diameter $NaYF_4$:Yb,Er nanosphere, 18 nm thick silica layer, and a 2.8 nm thick Au shell to achieve a maximum enhancement factor of 3.5 across the entire upconversion spectrum. Conversely, Kannan *et. al* [103] were able to selectively enhance portions of the emission spectrum of 35-nm-in-diameter UCNP by relying on a 20 nm thick metallic nanoshell composed of either Au or Ag to ultimately achieve a maximum enhancement factor of 22. However, no reports were found whereby core-shell architecture was used to simultaneously enhance both the absorption and emission aspects of the upconversion process.

This desired quality may be achieved by incorporating an additional metallic nanoshell into the previously considered core-shell architecture, creating doubly concentric nanometallic surfaces [97]. In addition, if the composition of these two plasmonic surfaces were differ-

ent, this would create an opportunity to combine the optical properties of both materials, resulting in unitary nanocomposite with a broadband optical response. This approach has been demonstrated theoretically in SiO_2@Ag@Au multilayer nanoparticles [110]; however, synthesizing these structures is practically elusive due to the fact that tangent Au and Ag nanoshells preferentially form alloys instead of distinct layers [111, 112], which disrupts the geometrically determined SPR. This problem is seemingly alleviated by an intervening dielectric layer that physically separates the metallic layers to inhibit contact alloying [113].

In an effort to apply MEF to the totality of the upconversion process, we present a preliminary investigation into broadband upconversion efficiency enhancements of $NaYF_4$:Yb,Er nanocrystals by amending the typical core-shell architecture to include Au-Ag bimetallic doubly concentric nanosurfaces. Morphological and spectral characterizations were performed on co-doped UCNPs encased in a silica shell. In particular, the addition of this dielectric layer, while incurring no discernible shift in the emission peak positions, was found to slightly enhance the energetically lower transition. Furthermore, the extinction spectra were calculated for two proposed multilayered nanostructures featuring bimetallic concentric nanosurfaces. Based on the results of these calculations, the potential for these nanostructures to enhance the entire upconversion process was determined.

4.3 Materials and Methods

4.3.1 Materials

Oleic acid (technical grade, 90%) and 1-octadecene(technical grade, 90%), CO-520 (average M_n 441), tetraethylorthosilicate (>99%), ammonia solution (28% ammonia) and $Na(CF_3OO)$ were purchased from Sigma Aldrich and used as received. $Y(CF_3OO)_3$, $Yb(CF_3OO)_3$, and

$Er(CF_3OO)_3$ were purchased from GFS chemicals and used as received.

4.3.2 Synthesis of upconverting nanoparticle core

The synthesis of Er^{3+} / Yb^{3+} doped $NaYF_4$ upconverting nanoparticles was carried out using a modified literature procedure [118]. In a typical reaction, 0.66 g $Na(CF_3OO)$, 1.875 g $Y(CF_3OO)_3$, 0.56 g $Yb(CF_3OO)_3$, and 0.056 g $Er(CF_3OO)_3$, are dissolved in a solution of 22.5 ml octadecene and 22.5 ml oleic acid. This resulting solution was stirred under vacuum at 100 °C for 45 minutes in a threenecked 500 ml round-bottomed flask to form a clear yellow solution. The round-bottomed flask was equipped with a water-jacketed condenser and the solution was flushed with argon for 5 minutes. The flask was lowered into a molten $NaNO_3/KNO_3$ (1:1 mass ratio) salt bath equilibrated at 342 °C and the solution was stirred vigorously with argon purge for 25 min. Then the reaction mixture was removed from the salt bath and cooled with an addition of 20 ml of octadecene. The upconverting nanoparticles were precipitated with the addition of 225 ml ethanol and isolated by centrifugation. The upconverting nanoparticles were redispersed in 270 ml of ethanol and isolated by centrifugation to ensure removal of starting materials. The nanoparticles were then redispersed in cyclohexane at a concentration of 50 mg/ml.

4.3.3 Deposition of silica spacer

A silica spacer was deposited on the Er^{3+} / Yb^{3+} doped NaYF4 upconverting nanoparticles using a modified literature procedure [77]. In a typical reaction, 2 ml of the upconverting nanoparticle dispersion in cyclohexane was added to 8 ml cyclohexane and 0.5 ml of CO-520. This mixture was stirred for 10 minutes, then 100 l of ammonia solution was added and the mixture was sonicated for 20 minutes yielding a clear solution. Then, 80 l of

tetraethylorthosilicate was added and the mixture was stirred at 600 rpm for 45h. The silica coated nanoparticles were precipitated by adding acetone, filtered, and rinsed twice with a 50:50 water:ethanol mixture. The silica coated nanoparticles were then redispersed in ethanol for optical analysis and transmission electron microscopy.

4.3.4 TEM measurements

Transmission electron microscopy (TEM) was performed using a Joel JEM 1400 instrument operating at an acceleration voltage of 80 kV. The TEM specimens were prepared by drop casting the hexane-dispersed nanoparticles onto the surface of a copper slot-style TEM grid.

4.3.5 Photoluminescence measurements

Spectral characterizations were performed using, as the excitation source, a pulsed Ti:Sapphire laser (Coherent Chameleon Ultra II) operating at 980 nm with a pulse duration of 140 fs and a repetition rate of 80 MHz. The average excitation power was controlled by an acousto-optical modulator and set to 30 mW for all measurements. A 40 mm aspheric lens was used to both excite and collect emissions from hexane or water UCNP dispersions contained in 1-cm-thick cells. With the aid of am 800 nm edge long-pass dichroic beam splitter, the photoluminescence (PL) was separated from the co-aligned excitation-emission beam. After this spectral separation, the PL was delivered, through a 100 μm wide slit, to a 0.55 m focal length spectrometer (HORIBA Jobin Yvon iHR550) equipped with a 600 grooves/mm, 500 nm blaze grating, and detected by a liquid-nitrogen cooled charged-coupled device (CCD) (HORIBA Jobin Yvon Symphony II).

4.3.6 SPR calculations

Extinction, scattering and absorption efficiencies for doubly concentric bimetallic nanosurfaces were calculated using a publicly available source code [114, 115] that applies Mie scattering theory to multilayered spheres using downward recursive algorithms developed by Yang [116]. Dielectric layers were assigned a constant index of refraction, n, of 1.55 while the optical responses of the Au and Ag layers were calculated from their reported dielectric functions [117].

4.4 Results and Discussion

4.4.1 Morpholocial and Spectral Characterization of UNCP@SiO_2 Precursors

The morphology and particle size of the bare and silica capped $NaYF_4$:Yb,Er nanocrystals were characterized by TEM studies. Figure 4.2 shows a bright-field TEM micrograph of a typical sample. The dimensions of this nanocomposite, (r_1, r_2), where r_1 indicates the radius of the UCNP, r_2 indicates the outer radius of the silica shell, and the shell thickness given by r_1-r_2, were determined to be approximately (10 nm, 75 nm).

The emissions from $NaYF_4$:Yb,Er are the result of a two photon absorption process mediated by the Yb^{3+} sensitizers in an energy transfer upconversion scheme [66, 78]. A ladder level illustrating this process is depicted in Figure 4.3. Upon the absorption of a 980nm (1.27 eV) photon, the Yb^{3+} ion is elevated from the ground state to the excited state of $^2F_{5/2}$. The Yb^{3+} ion relaxes back down to the ground state, transferring the energy of the excited state to the adjacent Er^{3+} ion, which, in turn, promotes the Er^{3+} from the ground state $^4I_{15/2}$

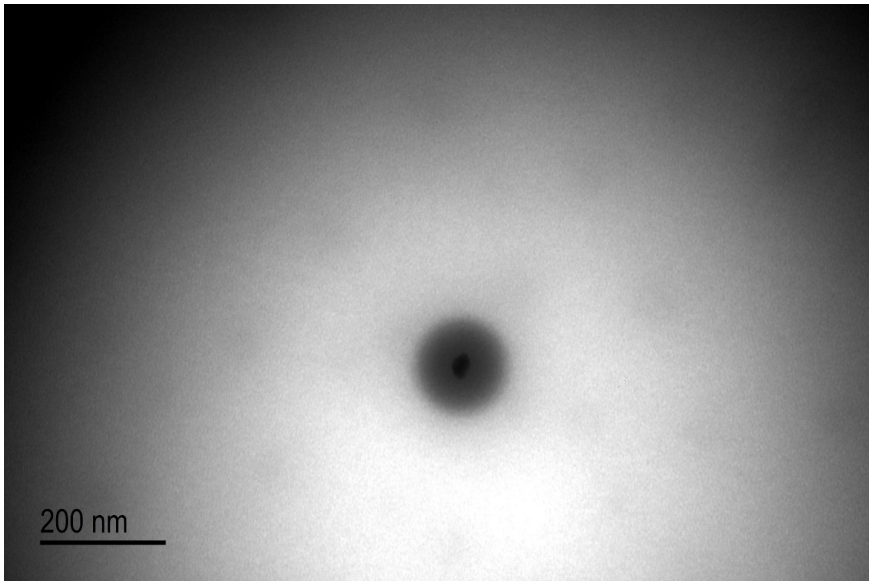

Figure 4.2: Bright-field TEM image of a typical silica-capped UCNP. The UCNP possesses a higher electron opacity than the silica layer and, as such, appears in the image as a dark core surround by the more transparent silica shell.

to the $^4I_{11/2}$ level. An absorption of a second photon populates the $^4F_{7/2}$ level, resulting from either a second energy transfer or by the direct excitation of the Er^{3+} ion. The Er^{3+} ion can then nonradiatively relax to the $^2H_{11/2}$ and $^4S_{3/2}$ levels from which it radiatively relaxes, resulting in the $^2H_{11/2} \rightarrow {}^4I_{15/2}$ and $^4S_{3/2} \rightarrow {}^4I_{15/2}$ green emission bands, centered 520 and 540 nm, respectively. Alternatively, the Er^{3+} can further nonradiatively relax from these levels to the $^4F_{9/2}$ level, ultimately producing the $^4F_{9/2} \rightarrow {}^4I_{15/2}$ red emission band centered at 660nm. In addition, there is an alternative optical route that can lead to this red emission. While in the $^4I_{11/2}$ state, the Er^{3+} ion can decay to the $^4I_{13/2}$ state and are then subsequently promoted to the $^4F_{9/2}$ state through an energy transfer from excited Yb^{3+} ions. Once again, radiative relaxation from this level produces the $^4F_{9/2} \rightarrow {}^4I_{15/2}$ red emission.

Figure 4.4 shows the emission spectra for UCNP and UCNP@ SiO_2 dispersed in hexane and water, respectively. Both spectra feature two strong emission bands at 545 and 660nm ($^2H_{11/2} \rightarrow^4 I_{15/2}$ and $^4F_{9/2} \rightarrow^4 I_{15/2}$, respectively, and a weak emission band at 520 nm

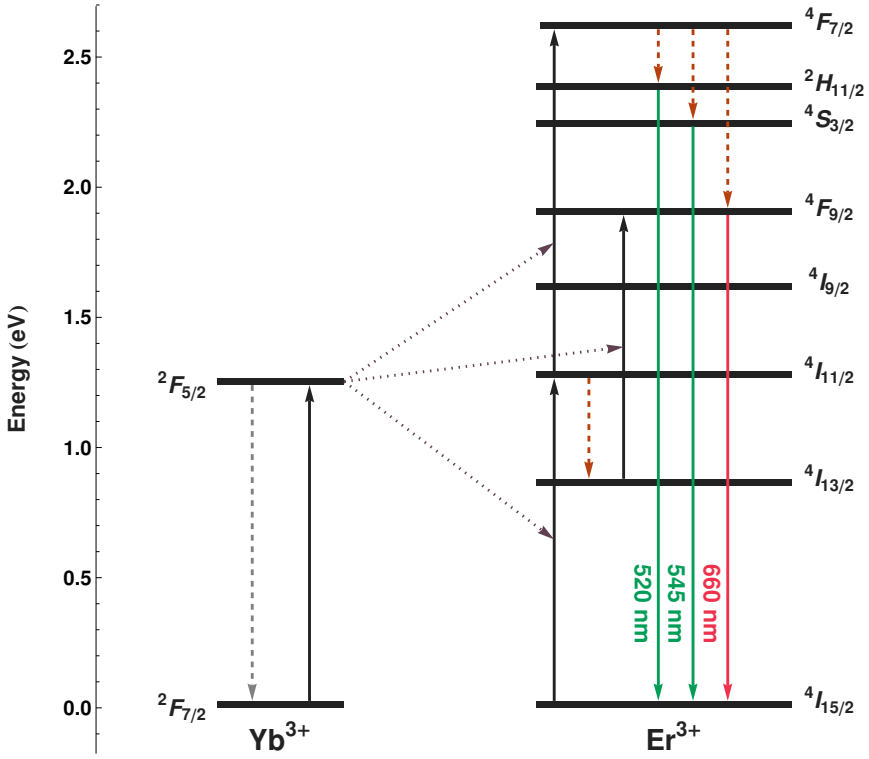

Figure 4.3: Energy state diagram depicting the relevant transitions in the upconversion process of co-doped $NaYF_4$:Yb,Er. Specifically, the energy level progressions that lead to the 520- and 540-nm green emissions, $^2H_{11/2} \rightarrow {}^4I_{15/2}$ and $^4S_{3/2} \rightarrow {}^4I_{15/2}$, and the 680-nm red emission, $^4F_{9/2} \rightarrow {}^4I_{15/2}$, are shown. Energy transfers, radiative relaxations, multiphonon-assisted non-radiative relaxations, and cross-relaxations are represented by purple-dotted, full, orange-dashed, and grey-dashed lines, respectively.

($^2H_{11/2} \rightarrow {}^4 I_{15/2}$). While the inclusion of the silica shell did not alter the peak positions or spectral shapes of these bands, it did result in the reduction of $R_{r/g}$, the intensity ratio between the 540 nm-centered green emission and the 680 nm-centered red emission, which contradicts the predicted behavior. The main expectation from the deposition of a silica shell onto the UNCP was the depletion of proximate surface quenching centers and their associated high vibrational quanta [87]. This would affect the phonon-assisted relaxations in the Er^{3+} activator and, hence, alter the relative populations of the excited states. Due to the greater reliance of the red upconversion pathways on nonradiative relaxations, particularly in the $^4I_{11/2} \rightarrow {}^4 I_{13/2}$ transition, the value of $R_{r/g}$ was expected to decrease in this case

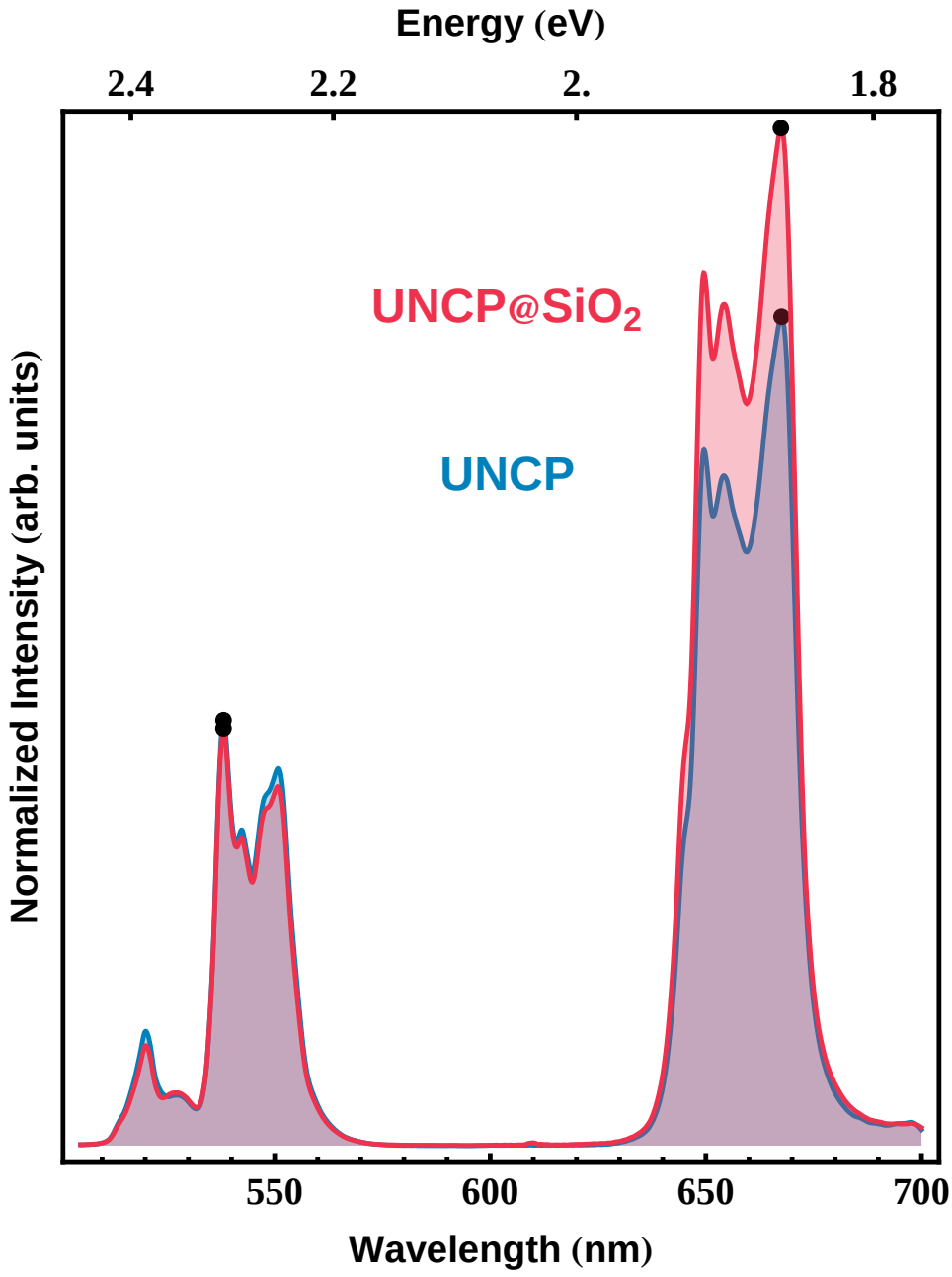

Figure 4.4: Normalized photoluminescence spectra of bare UCNPs (blue) and silica-coated UCNPs (red). The $R_{r/g}$ ratios for each spectrum were determined from the dominate peak intensities of the red and dominant-green bands, which were located at 538 and 654 nm, respectively (black dot). The $R_{r/g}$ value for bare UNCP was 1.95 while the value for UNCP@SiO_2 was 2.39.

[118, 119]. However, the opposite behavior was observed, with the $R_{r/g}$ ratio increasing from 1.95 to 2.39. This unanticipated outcome may be due to the corpulent silica shell layer that is well beyond the required thicknesses, 5-20 nm, for UNCP-metallic nanoshell separation. In contrast to their thinner counterparts, thick silica shells readily absorb the pump photons as well as the emitted upconverted photons, detrimentally affecting the luminescence yield; in addition, an amorphous silica shell suffers from considerable lattice mismatch with the UCNP core, producing interface defects that give rise to additional phonon modes [87] which, in turn, may selectively promote the red emission and lead to an increase in the $R_{r/g}$ ratio.

4.4.2 Calculated Extinction Spectra for Proposed Nanocomposites

Two proposed nancomposites for the heterointegration of $NaYF_4$:Yb,Er nanocrystals and concentric metallic nanosurfaces are presented in Figure 4.5, along with their generated extinction, scattering, and absorption efficiencies in water (n=1.33). Relying on the nomenclature of (r_{inner}, r_{outer}) to denote the inner and outer radii of a shell component, the first architecture features a doubly concentric metallic shell (DCMS) design (Fig. 4.5a) using the following compositional construction: Dielectric Core (0,20) nm @Au Shell (20,28) nm @Dielectric Shell (28,43) nm @Ag Shell (43,49) nm. The second architecture features a metallic core metallic shell (MCMS) design (Fig. 4.5b) using the following compositional construction: Ag Core (0,48) nm @Dielectric Layer (48,68) nm @Au Shell (68,83) nm. These dimensions were chosen not only to produce the desired SPR-related optical properties, but to also conform to empirically-determined optimal metallic thicknesses and inter-component spacing [99, 102, 103].

The extinction spectra for both architectures feature two primary bands, one residing in the visible region while the other resides in the near infrared region. This overall spectral profile

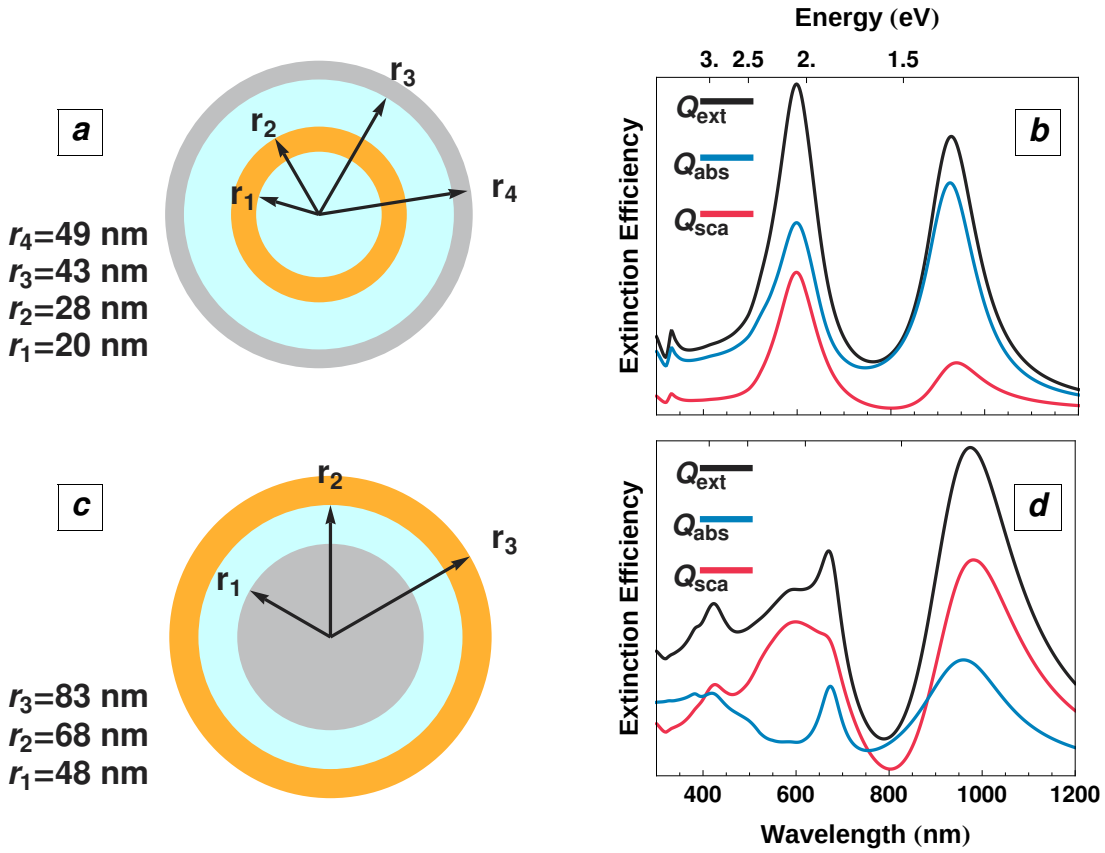

Figure 4.5: Proposed dielectric-metallic nanocomposites featuring doubly concentric bimetallic surfaces (left) along with their calculated extinction, absorption, and scattering efficiencies (right). DCMS and MCMS architectures (a and c) both possess extinction spectra (b and d) that overlap, to a certain degree, with both the absorption and emission band of$NaYF_4$:Yb,Er.

can largely be interpreted as the superposition of two plasma modes, one supported by the Au structure and the other supported by the Ag structure, and their subsequent spectral shifts due to the coupling between the modes. While mainly qualitative, this coupling can be understood in terms of the plasma hybridization framework, a theory analogous to molecular orbital theory [120]. Here, the plasmon response of complicated metal-based nanostructures originates from the interaction between the plasma modes of elementary structures from which those nanostructures are comprised. For instance, the plasma modes of a metallic nanoshell are the product of the interaction between the plasmons of a sphere and a cav-

ity, resulting in two new modes: a higher energy "antibonding" mode and a lower energy "bonding" mode". For the two designs presented, we are only concerned with the two lowest energy bonding modes of the combined bimetallic structures since the antibonding modes reside in the ultra-UV spectrum and are not germane to the present work. As depicted in Figure 4.6, this hybridization results in the lower energy band (in the near infrared region) being appreciably redshifted with respect to the outer shell plasmon mode for both architectures; in contrast, while the higher energy mode (in the visible region) for MCMS considerably redshifts with respect to the plasma mode of the Ag core, there is a relatively small shift for this mode in the DSMS case. This asymmetric behavior in the energy shifts for the latter case has been observed before and was attributed to phase retardation effects [120, 121]. In addition, the broadening and additional features in the lower energy band for the MCMS geometry is most likely due to the excitation of higher order multipole modes and their subsequent participation in the overall plasmon response [121].

Although the extinction efficiency spectra of both architectures overlap considerably with the absorption spectrum of the UCNPS, the degree of overlap with the emission spectra differs between the two designs. The MCMS configuration benefits from an overlap of the surface plasmon resonance with all three primary emission bands; in contrast, this overlap for DCMS appreciably occurs only for the bands centered at 540 and 680 nm. Hence, when considering the potential for MEF, the MCMS configuration is expected to affect the three major radiative transition by roughly the same degree, while the DCMS is expected to preferentially affect the $^2H_{11/2} \rightarrow {}^4I_{15/2}$ and $^4F_{9/2} \rightarrow {}^4I_{15/2}$ transitions. Despite this difference, both architectures possess the requisite SPR properties, namely the ability to affect both the absorption and emission aspect of the upconversion process in an MEF capacity. Furthermore, due to the nonlinear nature of the absorption process, the overlap with the absorption spectra of the UNCP is thought to be more influential in terms of

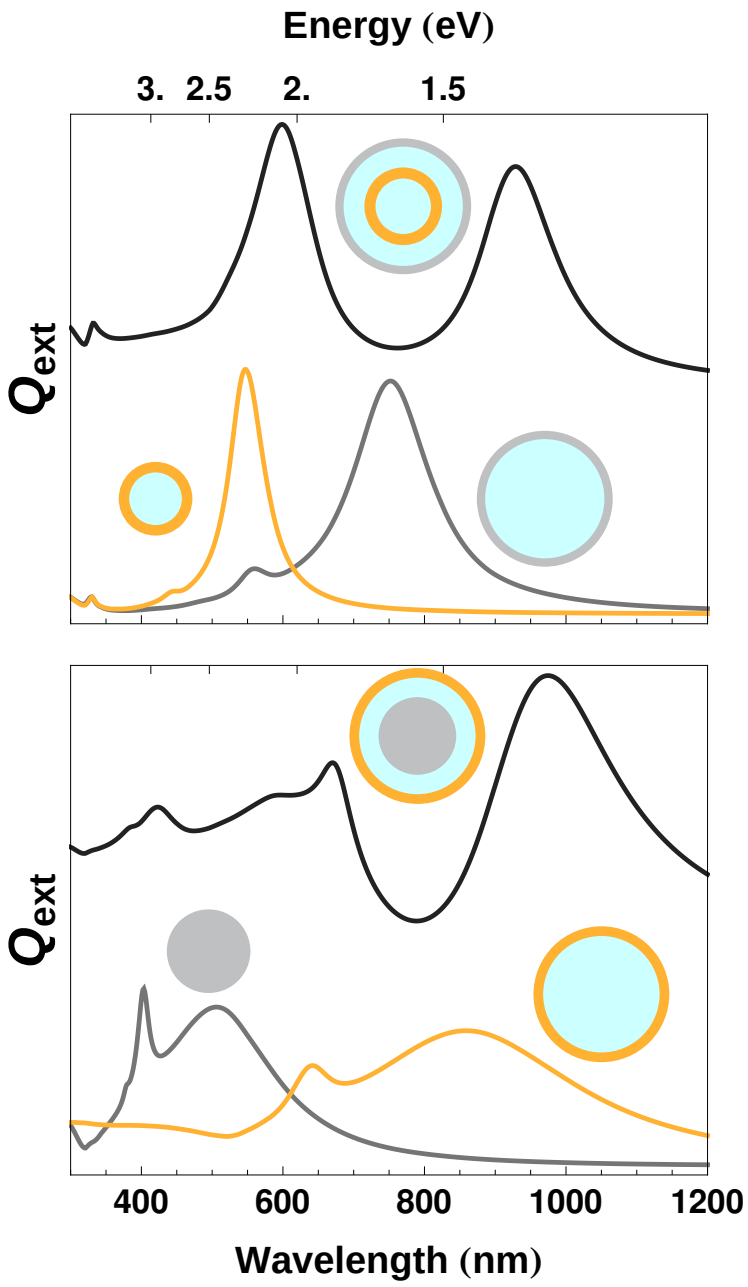

Figure 4.6: Comparison of extinction efficiencies between the proposed DSMS (a) and MCMS (b) architectures, and the elementary metallic structures from which those architectures are constructed. According to the plasma hybridization model, the extinction spectra of these concentric bimetallic structures are the result of plasmon mode coupling between the modes of the elementary structures, resulting in, among other effects, energy shifts between the modes of elementary and composite metallic structures.

MEF-related increases in fluorescence yields [72].

While the overall extinction spectra overlaps with the UC emission spectra, the absorption efficiency, Q_{abs}, has a greater contribution than the scattering efficiency, Q_{scat}, to the overall extinction efficiency of DCMS than MCMS. Recalling that scattering plasmon modes are largely responsible for MEF, the higher Q_{abs}/Q_{scat} ratio in the DCMS configuration will limit luminescence gains from MEF with respect to those of MSMS [95, 97]. In addition, although DCMS complements our current stage of nanocomposite synthesis, it suffers from a lack of biocompatibility and stability due to the silver exterior, in contrast to the Au exterior of the MCMS configuration [97, 122]; however, the former complication can be remedied through biomolecular surface capping agents such as DNA [77]. Lastly, when upconversion sensitizer-activator centers lie in the interspace between the metallic surfaces, as in the MCSM configuration, a greater enhancement in the excitation rate is expected due to the intense electric fields that have been theoretically predicted to reside in that region [123]. Hence, due to these advantages over DCMS, the MCS architecture stands as the current frontrunner for broadband metal-enhanced upconversion.

4.5 Conclusion

In summary, we have presented a preliminary study regarding the integration of upconverting $NaYF_4$:Yb,Er nanocrystals and concentric bimetallic nanosurfaces into a unitary nanocomposite with the purpose of enhancing the upconversion emissions through MEF. Precursors for these nanocomposites, bare UCNP and silica capped UCNP, were synthesized and subjected to structural and spectral analysis. While both nanoparticles produced the expected photoluminescence, the addition of a thick silica capping layer resulted in the redistribution of the primary emission bands in favor of the red emission, a possible consequence of inter-

face defects between the host matrix and the amorphous silica layer. In addition, extinction efficiencies were calculated for two proposed nanocomposites that rely on either DCMS or MCMS architecture. These nanocomposites feature two bimetallic concentric surfaces with geometrical parameters that produce plasmonic properties necessary for the metal-induced enhancement of both the excitation and emission aspects of the upconversion process. In terms of achieving this broadband MEF, the MCMS architecture was determined to be a more suitable candidate due to its plasmonic properties and compositional structure.

Chapter 5

Outcomes

5.1 Review and Conclusions

The works presented here have applied and demonstrated the relevance of optoperforation, spectral characterization of alloy disorder, and metal-enhanced fluorescence to systems that have largely been omitted from the purview of these techniques. In fact, the ultimate aim of these studies was not to develop novel experimental techniques, but to instead seek novelty in the application of routine techniques to previously overlooked systems for those techniques. For Chapters 2 and 3, these completed studies successfully administered the established methods of optoperforation and spectral characterization of alloy disorder to a vital, intact plant organism and an underrepresented III-V alloy, respectively; in the process, we satisfied the burden of proof that these methods can be expanded to include such systems while gleaning vital information about those systems. In Chapter 4, although the study is largely unfinished, we laid the groundwork for a metal-enhanced fluorescence study involving upconverting-bimetallic nanocomposites to achieve broadband enhancement of the upconversion emissions; this stands in contrasts to previous works which rely on monometallic

structures for narrowly tailored metal-induced enhancements.

Regarding optoperforation specifically, this technique has been demonstrated in a variety of single cell manipulation schemes, ranging from laser-mediate infiltration of exogenous material to precise laser ablation and cell knockout. However, these demonstrations have largely been restricted to mammalian cells, with plant protoplasts and calli being used in only a few reports. In Chapter 2, we expand these considered cellular systems to include intact plant organs by demonstrating femtosecond-laser-mediated infiltration of a membrane impermeable dextran-conjugated fluorophore into cells of vital *Arabidopsis* seedling stems. By monitoring the rate of dye uptake, and the reaction of CFP-expressing vacuoles and artificial cell walls, we adjusted both the intensity and exposure time of the perforating laser to values that preserved cell vitality and permitted the laser-assisted uptake of the fluorophore. By comparing these threshold values to those of previous studies that use mammalian cells, the exposure time was considerably reduced. This might be due to the rigid nature of the cell wall which may render it more susceptible to thermoelastic stress waves than the plasma membrane. By using these calibrated laser parameters, we were able to inject and later observe the long-term retention of dye in targeted cells, all without deleteriously affecting vital functions of those cells. Hence, we have provided a proof of principle study demonstrating that optoperforation can, indeed, be applied to intact, plant cells

In Chapter 3, we examined the excitonic radiative transitions of InAsP alloys through the lens of alloy disorder, in which local spatial variations of alloy components give rise to spectral broadening. While other III-V ternary alloys have been routinely examined in this capacity, InAsP alloys have not been subjected to the same research fervor and, as such, few reports exist concerning the spectral characterization of these alloys. As a result, the photoluminescence of excitonic transitions in two $InAs_xP_{1-x}$ alloys were studied through temperature and

magnetic field strength dependencies, as well as compositionally-dependent time-resolved behavior. The spectral shape, behavior of the linewidths at high magnetic fields, and divergence of the peak positions from band gap behavior at low temperatures indicated that alloy disorder exists in the x=0.40 composition while showing no considerable presence in the x=0.13 composition. In addition, although the measured temporal photoluminescence was spectrally unresolved, the longer lifetimes of the slow decay in x=0.40 may support the aforementioned findings, since carrier migration between localized states caused by alloy disorder would protract the radiative decay. Hence, the results of this work indicate that the alloy components in x=0.13 are homogeneously distributed, while those in x=0.40 are inhomogeneously distributed.

The metal-enhanced fluorescence study presented in Chapter 4 proposed retrofitting bimetalic nanostructures to lanthanide-doped upconverting nanocrystals in an effort to enhance a greater portion of the upconversion process than previous MEF-nanocomposite studies. This can be accomplished by tailoring the composition and geometry of the metallic portions of the nanocomposites to support plasmonic modes that resonantly enhance both the absorption and emission process of $NaYF_4$:Yb,Er. To this end, we diverged from the typical monometallic construction in favor of two architectures featuring Au-Ag bimetallic concentric surfaces, a decision that was substantiated by the calculated plasmon modes of these structures. Furthermore, we also demonstrated an ability to synthesize the precursors of these nanocomposites and verified that they possess the requisite upconversion photoluminescence spectrum. However, at this time, we have not managed to precisely control the thickness and crystalline nature of the silica layer. While this study is incomplete, we believe that we have presented both a convincing argument and preliminary data to support the continuation of this work to its timely conclusion.

5.2 Future Endeavors

During the course of each study, a number of extensions and further explorations had been considered. However, due to experimental, technical, and temporal constraints, they were not carried out. I include them here as a motivator and transition memorandum to guide future supplementations or entirely new investigations.

As already suggested, the optoperforation experiment is merely one that demonstrates proof of principle. For this approach to evolve past this categorization, applicability must be shown. Generally, optoperforation experiments involving biological systems are validated by successful transfection. Transfection involves injecting a cell with transgene-containing plasmids, leading to genetic modification of the cell, and, among many other outcomes, causing the cell to produce fluorescing proteins dictated by the transgenes [8]. These experiments have the benefit of showing that exogenous material has breached the cell boundary while preserving cell vitality, since the production of the foreign protein requires metabolic activity long after optical exposure. While optical transfection was briefly attempted in the *Arabidopsis* stem cells, these attempts were inconclusive, marred by the inability to differentiate the emissions of any fluorescing proteins from autofluorescence. Hence, proteins must be judiciously chosen for autofluorescence avoidance.

If transfection can be established, then this optoperforation procedure would become a legitimate technique for investigating local plant physiology. As such, this technique could be used for a variety of scientific pursuits, such as injecting a single developing cell with long-lived, immobile dye to monitor cell fate, or injecting trafficking compounds that can influence neighboring cells or elucidate intercellular transport pathways.

The primary shortcoming in the data acquisition of the InAsP photoluminescence was the inability to couple the streak camera to a spectrometer while maintaining sufficient through-

put of the collected photoluminescence. This would have granted the capacity to measure exciton radiative lifetimes as a function of emission energy and, as a result, provided information about the localization nature of the excitons. Lower energy emissions, originating from localized excitons, would exhibit protracted relaxations compared to the less-localized, higher energy transitions [52, 63]. Based on these energy dependent lifetimes, we would be able to verify our assertions regarding the observed lifetime reduction. Furthermore, this spectral information would help us discern the origins of the fast and slow decay.

In addition, exploratory etching could be performed to determine the effect that strain has on the various aspects of the photoluminescence spectrum for both compositions. By etching to subsurface epitaxial layers, especially to those experiencing significant strain due to lattice mismatch, strain-induced compositional shifts can be investigated to further characterize the epitaxial growth process [36]. Moreover, this exploratory etching may elucidate the origins of the lower energy transition in x=0.13, which has been attributed to impurity states. If this transition involves a donor level that is associated with a dislocation impurity, layers subjected to more strain would contain a higher density of these donor-like defects [46]. As a result, the lower energy emission would have a greater presence in the photoluminescence spectrum in these layers.

Lastly, an obvious addendum for this work would be to examine additional InAsP alloy compositions to determine the dependence of alloy disorder on the As/P incorporation ratio. According to theoretical and experimental evidence in other III-V ternary alloys, alloy broadening is expected to reach a maximum at an intermediate composition between the binary endpoints [124]. As such, based on the minimal presence of alloy disorder in x=0.13, a composition closer to InAs would be expected to have a similar absence of alloy disorder. In addition, excitonic linewidths for compositions between x=0.13 and x=0.40 can reveal the point in which alloy disorder starts become significant.

Since the MEF work involving upconverting nanoparticles is just in its nascent stages, the obvious next steps are those that help the project reach its desired conclusion: the incorporation of bimatallic concentric nanosurfaces for broadband plasmon-induced enhancements. The success of this endeavor hinges on the ability to deftly control the thicknesses and composition of each layer since these parameters determine the surface plasmon resonance modes. Therefore, the remaining challenges for this work are primarily those involving nanofabrication. However, the growth techniques for these metallic nanosurfaces have already been developed and thoroughly reported. Hence, the ability to execute these techniques will determine the overall success of the project.

However, if these challenges are met and these UCNP-bimetallic nanocomposites can, in fact, be synthesized, modifications to the luminescence yields may not necessarily be due to the metallic nanosurfaces. These yields can be attributed to a variety of other factors, such as differences in fluorophore concentrations or attenuation of the excitation source by different solvents. While these extenuating factors can be accounted for and controlled, MEF also possess a distinguishing feature: a reduction in emission lifetimes [91, 92]. Hence, lifetime measurements should be performed on these nanocomposites to verify metal-induced enhancements.

In addition, the effect of each dielectric or metallic layer on luminescence yields should be determined. This should be done to distinguish the role of each layer in any observed luminescence modifications as well as determine any interlayer interactions, such as plasmon hybridization.

Bibliography

[1] K. Nontapot, R.N. Kini, A. Gifford, T.R. Merritt, G.A. Khodaparast, T. Wojtowicz, X. Liu, and J.K.Furdyn, App. Phys. Lett. **90**, 143109 (2007).

[2] M. Bhowmick, T. R. Merritt, K. Nontapot, B. W. Wessels, O. Drachenko, and G. A. Khodaparast, Phys. Procedia **3**, 1167 (2009).

[3] M. Bhowmick, T.R. Merritt, G.A. Khodaparast, C. Feeser, B.W. Wessels, S.A. McGill, D. Saha, X. Pan, G. D. Sanders, and C. J. Stanton, AIP Conf. Proc. **1416**, 188 (2011).

[4] M. Bhowmick, T.R. Merritt, K. Nontapot, G.A. Khodaparast, T. D. Mishima, and M.B. Santos, AIP Conf. Proc. **1416**, 192 (2011).

[5] M. Bhowmick, T. R. Merritt, G. A. Khodaparast, B.W. Wessels, S.A. McGill, D. Saha, G.D. Sanders, and C.J. Stanton, Phys. Rev. B **85**, 125313 (2012).

[6] G. A. Khodaparast, Y. H. Matsuda, D. Saha, G. D. Sanders, C. J. Stanton, H. Saito, S. Takeyama, T. R. Merritt, C. Feeser, B. W. Wessels, X. Liu, and J. Furdyna, *Cyclotron resonance in ferromagnetic InMnAs and InMnSb*, Phys. Rev. B (*under review*).

[7] M.K. Hudait, Y. Zhu,N. Jain, S. Vijayaraghavan, A. Saha, T.R. Merritt ,G.A. Khodaparast, *In situ grown Ge in an arsenic-free environment for GaAs/Ge/GaAs heterostruc-*

tures on off-oriented (100) GaAs substrates using molecular beam epitaxy. J. Vac. Sci. Technol. B **30**, 051205 (2012).

[8] D. J. Stevenson, F. J. Gunn-Moore, P. Campbell, and K. Dholakia, J. R. Soc. Interface **7**, 863 (2010).

[9] R. Senz and G. Mller, Berich. Bunsen Gesell. **93**, 269 (1989).

[10] G. Weber, S. Monajembashi, J. Wolfrum, and K.-O. Greulich, Physiol. Plantarum **79**, 190 (1990).

[11] Y. A. Badr, M. A. Kereim, M. A.Yehia, O. O. Fouad, and A. Bahieldin, Photochem. Photobiol. Sci. **4**, 803 (2005).

[12] S. Eapen, Physiol. Mol. Biol. Plant **17**, 1 (2011).

[13] S. C. Jeoung, M. S. Sidhu, J. S. Yahng, H. J. Shin, and G. Y. Baik, Advances in Lasers and Electro Optics (InTech, 2010), Chap. 35.

[14] D. Fernando, J. Richards, and J. Kikkert, Plant Cell Rep. **25**, 450 (2006).

[15] H. Schinkel, P. Jacobs, S. Schillberg, and M. Wehner, Biotechnol. Bioeng. **99**, 244 (2008).

[16] Y. Barbashov, A. Zalesskii, A. Aibushev, O. Sarkisov, M. Radtsig, I. Khmel, O. Koksharova, and V. Nadtochenko, Nanotechnologies in Russia **6**, 668 (2011).

[17] W. Tang, D. A. Weidner, B. Y. Hu, R. J. Newton, and X.-H. Hu, Plant Sci. **171**, 375 (2006).

[18] T. Murashige, and F. Skoog, Physiol. Plant **15**, 473 (1962).

[19] G. Weber, S. Monajembashi, K. O. Greulich, and J. Wolfrum, Naturwissenschaften **75**, 35 (1988).

[20] B. K. Nelson, X. Cai, and A. Nebenfhr, Plant J. **51**, 1126 (2007).

[21] D. R. Hoagland and D. I. Arnon, Circular. California Agricultural Experiment Station **347**,1 (1950).

[22] A. Vogel, J. Noack, G. Httman, and G. Paltauf, Appl. Phys. B-Lasers O. **81**, 1015 (2005).

[23] S. Grill and E.H.K Stelzer, J. Opt. Soc. Am. A **16**, 2658 (1999).

[24] K. Konig, J Microsc-Oxford **200**, 83 (2000).

[25] G. F. Marshall and G.E. Stutz, "Handbook of Optical and Laser Scanning." (Marcel Dekker, 2005).

[26] X. Tsampoula, V. Garces-Chavez, M. Comrie, D. J. Stevenson, B. Agate, C. T. A. Brown, F. Gunn-Moore, and K. Dholakia, Appl. Phys. Lett. **91** 053902-3 (2007).

[27] P.T.C. So, C.Y. Dong, B. R. Masters, and K. M. Berland, Annu. Rev. Biomed. Eng. **2**, 399 (2000).

[28] C. Xu, R. M. Williams, W. Zipfel, and W. W. Webb, Bioimaging **4**, 198 (1996).

[29] Z. Li, S. Renneckar, and J. Barone, Cellulose **17**, 57 (2010).

[30] Ł. Piskorski, R.P. Sarzała, and W. Nakawaksi, Opto-Electron. Rev., **19**, 320 (2011).

[31] D. Elvira, R. Hostein, F. Bruno, L. Monniello, A. Michon, G. Beaudoin, R. Braive, I. Robert-Philip, I. Abram, I. Sagnes, and A. Beveratos, Phys. Rev. B, **84**, 195302 (2011).

[32] M. Wada and H. Hosomatsu, Appl. Phys. Lett., **64**, 1265 (1994).

[33] H. Sugiura, J. Cryst. Growth, **164**, 434 (1996).

[34] R.U. Martinelli, T.J. Zamerowksi, and P. A. Longeway, Appl. Phys. Lett., **54**, 277 (1989).

[35] H. Kosaka, A.A. Kiselev, F.A. Baran, K.W. Kim, and E. Yablonovitch, Electron. Lett., **37**, 464 (2001).

[36] S. G. Choi, and C. J. Palmstrøm, Y. D. Kim, D. E. Aspnes, and H. J. Kim and Yia-Chung Chang, App. Phys. Lett, **91**, 041917 (2007).

[37] M.K. Hudait, Y. Lin, and S.A. Ringel, J. of App. Phys., **105**, 061643 (2009).

[38] H. Ma, Z. Jin, L. Wang, and G. Ma, J. Appl. Phys., **109**, 023105 (2011).

[39] M. A. Meeker, B. A. Magill, T. R. Merritt, M. Bhowmick, K. McCutcheon, G. A. Khodaparast, J. G. Tischler, S. McGill, S. G. Choi, and C. J. Palmstrøm, Appl. Phys. Lett., **102**, 222102 (2013).

[40] L. Ji, S.L. Lu, Y.M. Zhao, M. Tan, J.R. Dong, and H. Yang, Journal of Crystal Growth, **363**, 44 (2013).

[41] H. Kaltz, *Optical Properties of III-V Semiconductors* (Springer-Verlag, Berlin, 1996).

[42] K.K. Bajaj, Mat. Sci. Eng. R., **34**, 59 (2001).

[43] P.S. Wang and B.W. Wessels, App. Phys. Lett., **44**, 766 (1984).

[44] K.H. Huang and B.W. Wessels, J. Cryst. Growth, **92**, 547 (1988).

[45] X. Liu, H. Jiang, G. Miao, H. Song, L. Cao, Z. Li, and D. Li, J. Alloy Compd., **506**, 530 (2010).

[46] R.V. Kruzelecky, C. Qiu, and D.A. Thompson, J. Appl. Phys., **75**, 4032 (1994).

[47] H. Q. Hou, C. W. Tu, and S.N.G. Chu, Appl. Phys. Lett., **58**, 2954 (1991).

[48] Y.G. Zhao, R.A. Masut, J.L. Brebner, C.A. Tran, and J.T. Graham, J. Appl. Phys., **76**, 5921 (1994).

[49] C.Y. Lee, M.C. Wu, H.P. Shiao, and W.J. Ho, J. Crystal Growth, **208**, 137 (2000).

[50] S.G. Choi, Ph.D. thesis, University of Minnesota, 2006.

[51] K.L. Letchworth and D.C. Benner, J. Quant. Spectrosc. Ra., **1073** 173 (2007).

[52] Y.H. Cho, G.H. Gainer, J.B. Lan, J.J. Song, W. Yang, and W. Jhe, Phys. Rev. B, **61**, 7203 (2000).

[53] E.F. Schubert, E.O. Göbel, Y. Horikoshi, K. Ploog, and H. J. Queisser, Phys. Rev. B, **30**, 813 (1984).

[54] B.H. Armstrong, J. Quant. Spectrosc. Ra., **7**, 61 (1967).

[55] K.P. O'Donnel and X. Chen, Appl Phys. Lett., **58**, 2924 (1991).

[56] M. Wada, S. Araki, T. Kudou, T. Umezawa, S. Nakajima, and T. Ueda, Appl. Phys. Lett., **76**, 2722 (2000).

[57] M. Grundmann and C.P. Dietrich, J. Appl. Phys., **106**, 123521 (2009).

[58] M. Hayne and B. Bansal, Luminescence, **27**, 179 (2012).

[59] R.A. Mena, G.B. Sanders, K.K. Bajaj, and S.C. Dudley, J. Appl. Phys., **70**, 1866 (1991).

[60] I. Vurgaftman, J.R. Meyer, and L.R. Ram-Mohan, J. Appl. Phys., **89**, 5815 (2001).

[61] S.K. Lyo, E.D. Jones, and S.R. Kurtz, J. Lumin., **60**, 409 (1994).

[62] S.M. Lee and K.K. Bajaj, J. Appl. Phys., **73**, 1788 (1993).

[63] H.S. Kim, R. Mair, J. Li, J. Lin, and H. Jang, J. Korean Phys. Soc., **37**, 391 (2001).

[64] J.X. Shen, Y. Oka, H.H. Cheng, F.Y. Tsai, and C.D. Lee, Superlattice Microst., **25**, 131 (1999).

[65] A. Amo, M.D. Martin, L. Klopotowski, L. Vina, A.I. Toropov, and K.S. Zhuravlev, Appl. Phys. Lett., **86**, 11906 (2005).

[66] F. Auzel, Chem. Rev., **104**, 139 (2004).

[67] D.M. Finlayson and B. Sinclair, *Advances in Lasers and Applications* (The Institute of Physics, London, 1999).

[68] J. W. Kim, J. I. Mackenzie, and W. A. Clarkson, Opt. Express, **17**, 11935 (2009).

[69] G. Wang, Q. Peng, and Y. Li, Acc. Chem. Res., **44**, 322 (2011).

[70] B.M. Van der Ende, L. Aartsa, and A. Meijerink, Phys. Chem. Chem. Phys., **11**, 11081 (2009).

[71] W. Zou, C. Visser, J.A. Maduro, M.S. Pshenichnikov, and J.C. Hummelen, Nature Photonics, **6**, 560 (2012).

[72] J. C. Goldschmidt, S. Fischer, H. Steinkemper, F. Hallermann, G. von Plessen, K. W. Kramer, D. Biner, and M. Hermle, IEEE Journal of Photovoltaic , **2**, 134 (2012).

[73] F. Wang. W.B. Tan, Y. Zhang, X. Fan, and M. Wang, Nanotechnology, **17**, R1 (2006).

[74] F. Wang. D. Banerjee, Y. Liu, X Chen, and X. Liu, Analyst, **135**, 1839 (2010).

[75] B.E. Cohen, Nature, **467**, 407 (2010).

[76] P. Yuan, Y.H. Lee, M.K. Gnanasammandhan, Z. Guan, Y. Zhang, and Q.H. Xu, Nanoscale, **4**, 5132 (2012).

[77] A. Priyam, N.M. Idris, and Y. Zhang, J. Matter. Chem., **22**, 960 (2012).

[78] H. Dong, L.D. Sun, and C.H. Yah, Nanoscale, **5**, 5703 (2013).

[79] F. Wang and X. Liu, Chem. Soc. Rev., **38**, 976 (2009).

[80] F. Wang and X. Liu, J. Am. Chem. Soc., **130**, 5642 (2008).

[81] H. Schafer, P. Ptacek, K. Kompe, and M. Haase, Chem. Matter, **19**, 1396 (2007).

[82] S. Schietinger, T. Aichele, H. Q. Wang, T. Nann and O. Benson, Nano Lett., **10**, 134 (2010).

[83] P.N. Prasad, *Nanophotonics*, (John Wiley & Sons, Inc., Hoboken, New Jersey, 2004).

[84] Q. Liu, W. Feng, T. Yang, T. Yi, and F. Li, Nature Protocols, **8**, 2033 (2013).

[85] J.C. Boyer and F. van Veggel, Nanoscale, **2**, 1427 (2010).

[86] C.H. Huang, *Rare Earth Coordination Chemistry: Fundamentals and Applications*, (John Wiley & Sons, Inc., Hoboken, New Jersey, 2010).

[87] D. Xie, H. Peng, S. Huang, and F. You, J. Nanomat., **2013**, 1 (2013).

[88] V. Kale, T. Soukka, J. Holsa, M. Lastusaari, J. Nanopart. Res. **15**, 1850 (2013)

[89] D.K. Williams, H. Yuan, and B.M. Tissue, **83**, 297 (1999).

[90] J.R. Lakowicz, K. Ray, M. Chowdhury, H. Szmacinski, Y. Fu, J. Zhang, and K. Nowaczyk, Analyst., **133**, 1308 (2008).

[91] C.D. Geddes and J.R. Lakowicz, J. Fluoresc., **2**, 121 (2002).

[92] R. Pribik, K. Aslan, Y.X. Zhang, and C.D. Geddes, J. Phys. Chem. C, **112**, 17969 (2008).

[93] K. Aslan, Y.X. Zhang, and C.D. Geddes, J. Appl. Phys., 084307 (2008).

[94] K. Aslan, Z. Leonenko, J.R. Lakowicz, and C.D. Geddes, J. Fluoresc., **15**, 643 (2005).

[95] F. Zhang, G.B. Braun, Y. Shi, Y. Zhang, Z. Sun, N.O. Reich, D. Zhao, and G. Stucky, J. Am. Chem. Soc., **132**, 2850 (2010).

[96] W.S. Chang, B.A. Willingham, L.S. Slaughter, B.P. Khanal, L. Vigderman, P. Natl. Acad. Sci. USA, **108**, 19879 (2011).

[97] C.S.S.R. Kumar, *UV-VIS and Photoluminescence Spectroscopy for Nanomaterials Characterization*, (Springer-Verlag, Berlin Hedelber, 2013).

[98] Z.Q. Li, S. Chen, J.J. Li, Q.Q. Liu, Z. Sun, Z.B. Wang, and S.M. Huang, J. Appl. Phys., **111**, 014310 (2012).

[99] M. Saboktakin, X. Ye, S.J. Oh, S.H. Hong, A.T. Faraman, U.K. Chettiar, N. Engheta, C.B. Murray, and C.R. Kagan, ACS Nano, **6**, 8759 (2012).

[100] J.W. Liaw, J.H. Chen, C.S. Chen, and M.K. Kuo, J. Opt. Soc. Am., **17**, 13532 (2009).

[101] W. Feng, L. D. Sun and C. H. Yan, Chem. Commun., 4393 (2009).

[102] P. Yuan, Y.H. Lee, M.K. Gnanasammandhan, Z. Guan, Y. Zhang, and Q.H. Xu, Nanoscale, **4**, 5132 (2012).

[103] P. Kannan, F. A. Rahim, X. Teng, R. Chen, H. Sun, L. Huang, and D.H. Kim, RSC Advances, **3**, 7718 (2013).

[104] P. Kannan, F.A. Rahim, R. Chen, X. Teng, L. Huang, H. Sun, and D.H. Kim, ACS Appl. Mater. Interfaces, **5**, 3508 (2013).

[105] R. Bardhan, N. K. Grady, J.R. Cole, A. Joshi, and N.J. Halas, ACS Nano 2009, **3**, 744 (2009).

[106] H. Zhang, Y. J. Li, I. A. Ivanov, Y. Q. Qu, Y. Huang and X. F. Duan, Angew. Chem., Int. Ed., **49**, 2865 (2010).

[107] L. Sudheendra, V. Ortalan, S. Dey, N.D. Browning, and I.M. Kennedy, Chem. Mater., **23**, 2987 (2011).

[108] J. Sun, H. Liu, D. Wu, B. Dong, and L. Sun, Mater. Chem. Phys., **137**, 1021 (2013).

[109] M. Fugjii, T. Nakano, K. Imakita, and S. Hayashi, J. Phys. Chem. C, **117**, 1113 (2012).

[110] D. Wu, X. Xu, and X. Liu, J. Chem. Phys., **129**, 074711 (2008).

[111] S. Link, Z.L. Wang, and M.A. El-Sayed, Phys. Chem. B, **103**, 3529(1999).

[112] M. Moskovits, I. Srnova-Sloufova, and B. Vickova, J. Chem Phys., **116**, 10435 (2002).

[113] X. Xia, Y. Liu, V. Backman, and G.A. Ameer, Nanotechnology, **17**, 5435 (2006).

[114] O. Pena and U. Pal, Comput. Phys. Commun., **180**, 2348 (2009).

[115] O. Pena-Rodriguez, P.P.G. Perez, and U. Pal, Int. J. Spectrosc., **2011**, 583743 (2011).

[116] W.Yang, Appl. Opt., **42**, 1710 (2003).

[117] P.B. Johnson and R.W. Christy, Phys. Rev. B, **6**, 4370 (1972).

[118] X. Ye, J.E. Collins, Y. Kang, J. Chen, D.T.N. Chen, A.G. Yodh, and C.B. Murray, P. Natl. Acad. Sci. USA, **107**, 22430 (2010).

[119] H.X. Mai, Y.W. Zhang, L.D. Sun, and C.H. Yan, J. Phys. Chem. C, **11**, 13721 (2007).

[120] E. Prodan, C. Radloff, N.J. Halas, and P. Nordlander, Science, **302**, 419 (2003).

[121] C. Radloff and N.J. Halas, Nano Lett., **4**, 1323 (2004).

[122] S.J. Oldenburg, J.B. Jackson, S.L. Westcott, and N.J Halas, Appl. Phys. Lett., **75**, 2897 (1999).

[123] T. Zhang, G. Lu, W. Li, J. Liu, L. Hou, P. Perriat, M. Martini, O. Tillement, and Q. Gong, J. Phys. Chem C, **116**, 8804 (2012).

[124] N. Nepal, J. Li, M.L. Nakarmi, J.Y. Lin, and H.X. Jiang, Appl. Phys. Lett.,**88**, 062103 (2006).

Appendix A

Voigt Fitting *Mathematica*$^{\mathrm{TM}}$ Script

```
(*GAUSS-HERMITE QUADRATURE APPROXIMATION OF VOIGT PROFILE*)

(*Golub-Welsch algorithm*)golubWelsch[d_?VectorQ,e_?VectorQ]:=
    Transpose[MapAt[(First[e] Map[First,#]^2)&,Eigensystem[
    SparseArray[{Band[{1,1}]->d,Band[{1,2}]->Sqrt[Rest[e]],Band
    [{2,1}]->Sqrt[Rest[e]]},{Length[d],Length[d]}]],{2}]]

(*Generates nodes and weights for Gauss-Hermite quadrature*)
ghq[n_Integer,prec_: MachinePrecision]:=Transpose[Sort[golubWelsch
    [ConstantArray[0,n],N[Prepend[Range[n-1]/2,Sqrt[Pi]],prec]]]]
(*Pre-tabulated G-H nodes and weights*)
gh=Prepend[Table[ghq[n,7],{n,2,41}],{{},{}}];
(*The function Vfgh[x,y,n] is the nth Gauss-Hermite quadrature
```

```
    approximation of the Voigt Profile*)
Vfgh[x_,y_,n_]:=(gh[[n,2,(n+1)/2]]y)/(\[Pi](y^2+x^2))+1/\[Pi] Sum
    [(2*gh[[n,2,i]]y(y^2+x^2+gh[[n,1,i]]^2))/((y^2+x^2+gh[[n,1,i
    ]]^2)^2-4x^2 gh[[n,1,i]]^2),{i,(n-1)/2}];


(*TAYLOR APPROXIMATION OF VOIGT PROFILE*)

(*Pre-tabulated values for the Taylor series coefficients in 0.01
    increments*)
W[x_,y_]=y/\[Pi] Convolve[Exp[-t^2],1/(y^2+t^2),t,x,Assumptions->
    y>0&&t\[Element]Reals];
K[x_,y_]=N@Re@W[x,y];
Kdx1[x_,y_]=N@Re@D[W[x,y],{x,1}];
Kdx2[x_,y_]=N@Re@D[W[x,y],{x,2}];
Kdx3[x_,y_]=N@Re@D[W[x,y],{x,3}];
Kdy1[x_,y_]=N@Re@D[W[x,y],{y,1}];
Kdy3[x_,y_]=N@Re@D[W[x,y],{y,3}];
Kdxy[x_,y_]=N@Re@D[W[x,y],x,y];
vtc=Table[{K[i,j],Kdx1[i,j],Kdx2[i,j],Kdx3[i,j], Kdy1[i,j],Kdy3[i,
    j],Kdxy[i,j]},{i,-5.5,5.5,0.01},{j,0,4,0.01}];

part[x_,y_]:=vtc[[1+100*(Floor[x+5.5,0.01]),1+100*Floor[y,0.01] ]]
floor1[x_?NumericQ]:=Floor[x,.01];
Derivative[1][floor1][x_]:=0
```

```
Derivative[2][floor1][x_]:=0
Derivative[1,0,0][part][x_,y_,n_]:=0;
Derivative[2,0,0][part][x_,y_,n_]:=0;
Derivative[0,1,0][part][x_,y_,n_]:=0;
Derivative[0,2,0][part][x_,y_,n_]:=0;
```

```
Vftaylor[x_?NumericQ,y_?NumericQ]:=(#1+(x-floor1[x])#2+(y-floor1[y
    ])#5+(x-floor1[x])(y-floor1[y])#7+.5((x-floor1[x])^2-(y-floor1[
    y])^2)#3+(1/6)(x-floor1[x])((x-floor1[x])^2-3(y-floor1[y])^2)
    #4-(1/6)(y-floor1[y])((y-floor1[y])^2-3(x-floor1[x])^2)#6)&
    @@part[x,y]
```

```
(*APPROXIMATION OF VOIGT FUNCTION AS PIECEWISE FUNCTION OF GAUSS-
    HERMITE QUADRATURE AND TAYLOR SERIES APPROXIMATIONS *)
VoigtProfile1[x_,\[Sigma]_,y_]:=Piecewise[{{N[Sqrt[Log[2]]]/(\[
    Sigma]*N[Sqrt[\[Pi]]]) Vftaylor[x,y],y-5.3<=x<=5.3-y&&0<=y
    <=3.75},{N[Sqrt[Log[2]]]/(\[Sigma]*N[Sqrt[\[Pi]]]) Vfgh[x,y,7],
    y>0}}]/.{x->N[Sqrt[Log[2]]] x/\[Sigma]};
(*DataEv[x1,x2,x3] (x1,x2,x3 are integers) extracts the x2-th and
    x3-th column of the matrix "DataRaw" (CCD data of the
    photoluminescence spectrum), converts the x2-th row from units
    of nm to eV, and creates a list of ordered pairs {eV, intensity
```

```
    } called Datax1. Then, DataEv creates a ListPlot of Datax1 and
    the user Alt-left-clicks on the graph to create Locators (the
    first Locator is produced with just a left-click). Every 3
    Locators are used to indicate a single Voigt profile, where the
     first locator indicates the profile's peak position, and the
    distance between the last two Locators indicates the linewidth
    of the profile. The positions of the Locators are partitioned
    into a list of 3 ordered pairs and this partitioned list is
    stored as "criticalpts" *)
DataEv[x1_,x2_,x3_]:=Module[{a=x1,s=x2, d=x3,f},
f=Table[{1239.84193/DataRaw[[i, s]], DataRaw[[i,d]]},{i,3,
    Dimensions[DataRaw][[1]]}];
Clear@Evaluate@StringJoin["Data",ToString[a]];
Evaluate@ToExpression@
StringJoin["Data",ToString[a]]=f;
Manipulate[criticalpts=Partition[pts,3];Row[{ListPlot[f,PlotRange
    ->All,ImageSize->400],Text[Grid[Partition[pts,3],Frame->All
    ]]},{{pts,{{Center,Center}}},Locator,Appearance->Graphics[{Red
    ,Disk[{0,0}]},ImageSize->10],LocatorAutoCreate->{2,10}}]]

(*VoigtGuess[x1,x2,x3] (x1, x2 are integers, x3 is a list)
    generates a Manipulate output that allows one to adjust the
    values of peak position, half-linewidths and amplitudes of each
     voigt profile of a given spectra, and these values are stored
    in "guesspts". The Manipulate is initialized with those guess
```

```
    values obtained from the DataEv function. x1 is the data
    signifier (for example, if the list containing spectrum data is
     called Data04, then x1 is 04); x2 dictates whether to use the
    guess values obtained from DataEv (x2=0) or to use x3 guess
    values (x2!=0)*)

VoigtGuess[x1_,x2_,x3_]:=Module[{A,S,lta,ltb,listGuess,listFitvar,
    listParameters,VoigtProfile,prevBestFitGuess,listManipGuess},

A=Evaluate@ToExpression@StringJoin["Data",ToString[x1]];
listGuess={#[[1,1]],Abs[(#[[3,1]]-#[[2,1]])]/2.35,1,Abs[#[[1,2]]-
    Min@A[[All,2]]]/100}&/@criticalpts;
listFitvar=Array[ToExpression@StringJoin["a",ToString[Row
    [{##}]]]&,{Dimensions[listGuess][[1]],4}];
listParameters=Evaluate@Partition[Flatten[{listFitvar,listGuess
    },{{2,3,1}}],2];

VoigtProfile[x_,\[Sigma]_,y_]=Piecewise[{{N[Sqrt[Log[2]]]/(\[Sigma
    ]*N[Sqrt[\[Pi]]]) Vftaylor[x,y],y-5.3<=x<=5.3-y&&0<=y<=3.75},{N
    [Sqrt[Log[2]]]/(\[Sigma]*N[Sqrt[\[Pi]]]) Vfgh[x,y,7],y>0}}]/.{x
    ->N[Sqrt[Log[2]]] x/\[Sigma]};

lta={{#[[1]],N[#[[2]],4]},0,2*N[#[[2]],4]}&/@listParameters;
ata=Min@A[[All,1]];
atb=Max@A[[All,1]];
```

```
atc=Min@A[[All,2]];
atd=Max[100#[[4]]&/@listGuess];
prevBestFitGuess=If[x2==1,0,Partition[Flatten[{listFitvar,
    Partition[x3,4]},{{2,3,1}}],2]];

listManipGuess=If[x2==1,Partition[listParameters,4],Partition[
    prevBestFitGuess,4]];


ReleaseHold@ToExpression["Manipulate[guesspts="<>ToString[
    Evaluate@listFitvar]<>"; Show["<>ToString[ListPlot[A,PlotRange
    ->{Full,{atc-1.6*atd,atc+1.3*atd}},AxesOrigin-> {Automatic,atc
    -1.6*atd},PlotStyle->PointSize[.0005]],StandardForm]<>",Plot
    ["<>ToString[y0+Total[#[[4]]*VoigtProfile[(x-#[[1]])
    ,#[[2]],#[[3]]]&/@Array[ToExpression@StringJoin["a",ToString[
    Row[{##}]]]&,{Dimensions[listGuess][[1]],4}]],TraditionalForm
    ]<>",{x,ata,atb},PlotRange->All,PlotStyle->{Orange}],"<>
"Plot["<>ToString[(y0-1.3*atd+#[[4]]*VoigtProfile[(x-#[[1]])
    ,#[[2]],#[[3]]])&/@Array[ToExpression@StringJoin["a",ToString[
    Row[{##}]]]&,{Dimensions[listGuess][[1]],4}],TraditionalForm
    ]<>",{x,ata,atb},PlotRange->All"<>"]"
<>",ImageSize->500],"<>StringReplace[ToString[Append[Prepend[
Flatten
    [{{{#[[1,1]],#[[1,2]]},0.95#[[1,2]],1.05#[[1,2]],.0001#[[1,2]]},{{#[[2,1]]
    Delimiter}&/@listManipGuess,1]
```

```
,start],end],InputForm],{"{start,"->"","  end}"->""}]<>",{{y0,atc
    },.9*atc,1.1*atc}"<>"]"]



];

(*Vfit[x1] (x1 is an integer) is the Voigt Fitting Protocol,
    fitting the data in Datax1 to the VoigtProfile function and
    producing a graphical representation of the fitting results.
    The guess values for NonlinearModelFit are the final maniuplate
     values (stored in "guesspts") of the VoigtGuess output*)
VFit[x1_]:=Module[{A,S,listGuess,listFitvar,listParameters,
    VoigtProfile,VFittedPeaksSeparated,graphFit,
    listMaxPeaksSeparated},

A=Evaluate@ToExpression@StringJoin["Data",ToString[x1]];
listGuess=guesspts;
listFitvar=Array[ToExpression@StringJoin["a",ToString[Row
    [{##}]]]&,{Dimensions[listGuess][[1]],4}];
listParameters=Evaluate@Partition[Flatten[{listFitvar,listGuess
    },{{2,3,1}}],2];
VoigtProfile[x_,\[Sigma]_,y_]=Piecewise[{{N[Sqrt[Log[2]]]/(\[Sigma
    ]*N[Sqrt[\[Pi]]]) Vftaylor[x,y],y-5.3<=x<=5.3-y&&0<=y<=3.75},{N
    [Sqrt[Log[2]]]/(\[Sigma]*N[Sqrt[\[Pi]]]) Vfgh[x,y,7],y>0}}]/.{x
```

```
    ->N[Sqrt[Log[2]]] x/\[Sigma]};
ata=Min@A[[All,1]];
atb=Max@A[[All,1]];
atc=Min@A[[All,2]];
atd=Max[100#[[4]]&/@listGuess];
S=NonlinearModelFit[A,y0+Total[#[[4]]*VoigtProfile[(x-#[[1]])
    ,#[[2]],#[[3]]]&/@Array[ToExpression@StringJoin["a",ToString[
    Row[{##}]]]&,{Dimensions[listGuess][[1]],4}]],AppendTo[
    listParameters,{y0,Min@A[[All,2]]}],x,AccuracyGoal->4,
    MaxIterations->200];

Clear@Evaluate@StringJoin["VFitted",ToString[x1]];
Evaluate@ToExpression@StringJoin["VFitted",ToString[x1]]=S;

Clear@Evaluate@StringJoin["bf",ToString[x1]];
Evaluate@ToExpression@StringJoin["bf",ToString[x1]]=Chop@S["
    BestFitParameters"];

VFittedPeaksSeparated[x_]=((y0+-1.3*atd+#[[4]]*VoigtProfile[(x
    -#[[1]]),#[[2]],#[[3]]])&/@listFitvar)/.Chop@S["
    BestFitParameters"];
listMaxPeaksSeparated={#[[1]],VFittedPeaksSeparated
    [#[[1]]][[#[[5]]]]}&/@Join[Partition[Chop@S["BestFitParameters
    "][[All,2]],4],{#}&/@(Range[Dimensions[Partition[Chop@S["
    BestFitParameters"][[All,2]],4]][[1]]),2];
```

```
graphFit=Show[ListPlot[A,PlotRange->{Full,{atc-1.6*atd,atc+1.3*atd
    }},AxesOrigin-> {Automatic,atc-1.6*atd},PlotStyle->{Black,
    PointSize[.002]},AxesLabel->{Style["Energy (eV)",FontFamily->"
    Helvetica"]}],
Plot[(y0+Total[#[[4]]*VoigtProfile[(x-#[[1]]),#[[2]],#[[3]]]&/
    @Array[ToExpression@StringJoin["a",ToString[Row[{##}]]]&,{
    Dimensions[listGuess][[1]],4}]])/.Chop@S["BestFitParameters"],{
    x,Min@A[[All,1]],Max@A[[All,1]]},PlotStyle->{Red,Thick,Opacity
    [0.5]},PlotRange->All],Plot[Evaluate[VFittedPeaksSeparated[x
    ]],{x,Min@A[[All,1]],Max@A[[All,1]]},PlotRange->Full,PlotStyle
    ->ColorData[1,"ColorList"]],Graphics[Flatten[{Black,Point[
    listMaxPeaksSeparated[[(#[[5]])]]],Black,Text[Style[ToString
    [#[[5]]],FontSize->10,FontFamily->"Helvitica",Bold],
    listMaxPeaksSeparated[[(#[[5]])]]+{0,2./35. ((atc+1.3*atd)-(atc
    -1.6*atd))}]}]&/@Join[Partition[Chop@S["BestFitParameters"][[
    All,2]],4],{#}&/@(Range[Dimensions[Partition[Chop@S["
    BestFitParameters"][[All,2]],4]][[1]]]),2]],PlotRange->All];


Row[{Show[graphFit,ImageSize->500],Spacer[20],Column[{Text[Style[
    Grid[{{"Adjusted R^2",ToString[S["AdjustedRSquared"]]}},Frame->
    All],FontSize->15,FontFamily->"Helvitica"]],
Text[Style[Grid[Prepend[Join[{#}&/@(Range[Dimensions[Partition[
    Chop@S["BestFitParameters"][[All,2]],4]][[1]]]),Partition[
    Chop@S["BestFitParameters"][[All,2]],4],2],{"Peak #","Center (
```

```
    eV)","\[Sigma] (eV)","y","Amp Coeff"}],Frame->All],FontSize
    ->15,FontFamily->"Helvitica"]]}]}]
]
```